Received: 27 October 2021 | Revised: 11 May 2022 | Accepted: 16 June 2022

DOI: 10.1002/nag.3417

RESEARCH ARTICLE

WILEY

A novel coupled NS-PFEM with stable nodal integration and polynomial pressure projection for geotechnical problems

Ze-Yu Wang[2,3] | **Yin-Fu Jin**[1] | **Zhen-Yu Yin**[2] | **Yu-Ze Wang**[3]

[1]College of Civil and Transportation Engineering, Shenzhen University, Shenzhen, Guangdong, China

[2]Department of Civil and Environmental Engineering, The Hong Kong Polytechnic University, Hung Hom, Kowloon, Hong Kong, China

[3]Department of Ocean Science and Engineering, Southern University of Science and Technology, Shenzhen, Guangdong, China

Correspondence
Yin-Fu Jin, College of Civil and Transportation Engineering, Shenzhen University, Shenzhen, 518060 Guangdong, China.
Email: yinfu.jin@polyu.edu.hk

Funding information
the Research Grants Council (RGC) of Hong Kong Special Administrative Region Government (HKSARG) of China, Grant/Award Numbers: 15209119, R5037-18F; The Hong Kong Polytechnic University Strategic Importance Fund (ZE2T); Project of Research Institute of Land and Space (CD78)

Abstract

The node-based smoothed particle finite element method (NS-PFEM) offers high computational efficiency but is numerically unstable due to possible spurious low-energy mode in direct nodal integration (NI). Moreover, the NS-PFEM has not been applied to hydromechanical coupled analysis. This study proposes an implicit stabilised T3 element-based NS-PFEM (stabilised node-based smoothed particle finite element method [SNS-PFEM]) for solving fully hydromechanical coupled geotechnical problems that (1) adopts the stable NI based on multiple stress points over the smooth domain to resolve the NI instability of NS-PFEM, (2) implements the polynomial pressure projection (PPP) technique in the NI framework to cure possible spurious pore pressure oscillation in the undrained or incompressible limit and (3) expresses the NI for assembling coefficient matrices and calculating internal force in SNS-PFEM with PPP as closed analytical expressions, guaranteeing computational accuracy and efficiency. Four classical benchmark tests (1D Terzaghi's consolidation, Mandel's problem, 2D strip footing consolidation and foundation on a vertical cut) are simulated and compared with analytical solutions or results from other numerical methods to validate the correctness and efficiency of the proposed approach. Finally, penetration of strip footing into soft soil is investigated, showing the outstanding performance the proposed approach can offer for large deformation problems. All results demonstrate that the proposed SNS-PFEM with PPP is capable of tracking hydromechanical coupled geotechnical problems under small and large deformation with different drainage capacities.

KEYWORDS
hydro-mechanical coupling, large deformation , PFEM, polynomial pressure projection, stable nodal integration

1 | INTRODUCTION

Hydromechanical coupling has always been a major issue in geotechnical research, because the interaction between deformable solid skeleton and pore fluid flow dominates many engineering problems, such as long-term consolidation settlement,[1] rainfall-induced landslides,[2] internal erosion[3,4] and embankment construction.[5] Most such problems prominently exhibit an obvious large-deformation feature. Numerical tools based on the finite element method (FEM) have long been developed to simulate such coupled geotechnical problems.[1,3,4,6–10] However, it is well-known that several intrinsic

defects of FEM would hinder its ultimate application.[11–14] For example, the accuracy and convergence of FEM solution can be greatly influenced by the mesh distortion. Traditional FEM with low-order element (e.g., T3 element) tends to give overly stiff solution and incur the volumetric locking when treating nearly incompressible solid, which requires specific numerical techniques (e.g., B-bar method[11,14]) to fix. Meshfree methods could reduce the influence of mesh quality in hydromechanical modelling[15–19] but would introduce more trouble in the implementation of boundary conditions and more computational cost in the evaluation of interpolation functions and derivatives.[20,21] a highly efficient hydromechanical coupling approach that benefits from the accuracy of traditional FEM and the large deformation ability of meshfree method is worth studying.

The smoothed finite element method (S-FEM) based on the gradient smoothing technique is believed to be able to introduce some advantages of meshfree methods into the low-order FEM interpolation scheme.[22–24] The idea of using both displacements and strains with some smoothing can trace back to the Taylor–Galerkin FEM,[25–27] mixed stabilised FEM,[28,29] stabilised conforming nodal integration (NI) in meshfree methods,[30–32] and then this idea was adopted in the linear point interpolation setting.[20,23,33] The smoothing domain in S-FEM usually brings into information from all adjacent elements and makes the solution more accurate than FEM.[20,34] The use of variable mapping with Jacobian matrices is also reduced or avoided, which makes S-FEM work well with heavy mesh distortion.[20,35] Besides, S-FEM tends to give 'softer' solution which could alleviate the overly stiff problem of FEM with linear triangular element.[20,33–35] Different ways of constructing the smoothing domain have given rise to several methods, including cell-based S-FEM (CS-FEM), edge-based S-FEM (ES-FEM) and node-based FEM (NS-FEM), most of which have been introduced into the simulation of solid-fluid interaction problems.[8,36–39] Considering the requirements of large deformation analysis, S-FEM could be extended into an updated Lagrangian approach called the smoothed particle FEM (S-PFEM), which has recently shown great suitability for simulating some unconventional geotechnical problems.[40–44] In S-PFEM, all the nodes are movable and regarded as a particle cloud discretising the calculation domain, with their connectivity repeatedly rebuilt using certain triangulation and boundary identification techniques. In particular, the NS-FEM could be conveniently improved to the node-based smoothed particle FEM (NS-PFEM). Because all the essential variables in NS-FEM are characterised by node-based smoothing domain, accuracy loss due to the variable mapping between quadrature points and particles—common in traditional particle FEM (PFEM) and edge-based smoothed particle FEM (ES-PFEM)—could be avoided. However, descriptions of the development and application of hydromechanical coupled NS-FEM are scant, except in some papers[38,39] that give primary construction. Besides, the skills needed for pore pressure stabilisation and the potential for large deformation analysis still require further investigation and improvement in NS-PFEM.

Direct NI in NS-PFEM tends to incur the numerical instability due to spurious zero-energy mode, which comes from the violation of integration constraint conditions.[18,19,30,45] Recently, a stabilisation scheme based on a locally linear strain assumption was proposed and applied in several mechanical problems,[46–49] for which circle domains and quadrature points must be identified to allow gradient evaluation. Meanwhile, a similar approach of adding more stress points in the subdomains[30,45,50] is seemingly worth consideration when constructing a stabilised node-based smoothed particle finite element method (SNS-PFEM) method, because no extra evaluations of subdomain gradient is required in the 3-node triangulation interpolation (T3) scheme.

Furthermore, nonphysical pore pressure oscillation is another tough issue in hydromechanical coupling problems, especially when dealing with the undrained incompressible limit, that is, the conditions of low permeability and very short periods.[12,14,51,52] This is because a discrete inf-sup Ladyzhenskaya–Babuška–Brezzi (LBB) condition does not hold for some interpolation pair of $\mathbf{u}$ the solid displacement and p the fluid pressure,[53,54] especially the equal-order T3 element adopted in SNS-PFEM. Many stabilisation strategies have been developed such as separate interpolations for coupled physical fields,[51] modifying the pressure equation by the divergence of momentum equation,[55] finite-incremental calculus formulation,[56,57] Galerkin least square technique,[58] fractional step methods,[59] enhanced strain formulations,[60] to name a few. But these are either difficult in code modification or depend on sophisticated element construction that is infeasible in a mesh-updating framework. The polynomial pressure projection (PPP) technique as a remedy to violation of LBB conditions,[19,52,54] fortunately, offers a convenient approach that can be used in all the common interpolation schemes, with only a relatively minor modification needed to the discretised equations. It has been widely applied in many similar numerical problems that require pressure stabilisation, such as low permeable porous medium,[19] incompressible solid[35] and Stokes flow equation,[61] and has proven to be highly efficient. Thus, the PPP is worth to be implemented in the SNS-PFEM framework to stabilise the possible fluid pressure oscillation.

This paper is organised as follows. In Subsections 2.1–2.2, the fully coupled hydromechanical numerical formulation is established, with a detailed description of the governing equations in strong and weak forms, spatial discretisation based on FEM-T3 interpolation and an implicit temporal discretisation θ method. Subsections 2.3–2.5 introduce the principles of

the gradient smoothing technique with stabilised NI, the PPP method and the particle method via the remeshing strategy. NI for stabilised equations and PPP is derived to closed formulations in detail. Several benchmark tests with reference solutions are implemented in Section 3, with the correctness and efficiency of the proposed SNS-PFEM validated and analysed by comparison with reference solutions. Finally, a hydromechanical coupled large deformation simulation of rigid footing penetration into soft soil is investigated in Section 4. The vertical reaction force–displacement curve and other responses are presented and analysed to show the advantages of the proposed coupled SNS-PFEM.

2 | HYDRO-MECHANICAL COUPLED SNS-PFEM

2.1 | Strong and weak forms of governing equations

The momentum balance equation of deformable soil skeleton together with the effective stress principle is expressed as Equation (1). The fluid is incompressible which obeys the linear Darcy's rule in the porous medium, leading to the mass conservation equation by combining Equations (2) and (3),

$$\nabla \cdot (\boldsymbol{\sigma}' - p\mathbf{I}) + \mathbf{b} = \mathbf{0} \tag{1}$$

$$\nabla \cdot \mathbf{u} + \nabla \cdot \mathbf{q}_f = 0 \tag{2}$$

$$\mathbf{q}_f = -\frac{\mathbf{k}}{\gamma_f} \cdot \nabla p \tag{3}$$

where $\boldsymbol{\sigma}\prime$is the effective stress tensor, $\mathbf{I}$ the identity tensor, $\mathbf{b}$ the body force in the medium, $\mathbf{q}_f$ the Darcy velocity of fluid flux, γ_f the unit weight of fluid, $\mathbf{k}$ the hydraulic conductivity tensor, $\mathbf{u}$ the solid displacement field and p is the fluid pressure field. $\mathbf{u}$ and p act as the primary unknowns in the hydromechanical coupling. The dot of $\dot{\mathbf{u}}$ and other variables in this paper denotes the time derivative.

The infinitesimal strain tensor is expressed as Equation (4). The nonlinear constitutive model is written as in Equation (5), where $\mathbb{D}_{ep}$ is the fourth-order elastoplastic tangential moduli.

$$\boldsymbol{\varepsilon} = \nabla^s \mathbf{u} = \frac{1}{2}(\nabla \mathbf{u} + \nabla \mathbf{u}^T) \tag{4}$$

$$\dot{\sigma} = \mathbb{D}_{\text{ep}} : \dot{\varepsilon} \tag{5}$$

The natural and essential boundary conditions are exhibited in Equation (6), namely displacement boundary Γ_u, traction boundary Γ_t, fluid pressure boundary Γ_p and imposed flow flux boundary Γ_q. The complementary conditions in Equation (7) must be satisfied.

$$\begin{cases} \mathbf{u} = \bar{\mathbf{u}} \text{ on } \Gamma_u \\ \mathbf{n} \cdot \boldsymbol{\sigma}' = \bar{\mathbf{t}} \text{ on } \Gamma_t \\ p = \bar{p} \text{ on } \Gamma_p \\ -\mathbf{n} \cdot \mathbf{q}_f = \bar{q} \text{ on } \Gamma_q \end{cases} \tag{6}$$

$$\Gamma = \Gamma_u \cup \Gamma_t = \Gamma_p \cup \Gamma_q, \Gamma_u \cap \Gamma_t = \emptyset, \Gamma_p \cap \Gamma_q = \emptyset \tag{7}$$

As the prerequisite for deriving FEM equations, the equivalent weak forms of aforementioned partial differential equations together with the boundary conditions are stated in Equations (8) and (9), where $\mathbf{u}$,p and their variations $\delta\mathbf{u}$ and δp are defined in appropriate trial function spaces S_u, $S_p$and test function spaces V_u, V_p.

$$\mathcal{L}_u = \int_\Omega (\nabla^s \delta\mathbf{u} : \boldsymbol{\sigma}' + p\nabla \cdot \delta\mathbf{u} - \delta\mathbf{u} \cdot \mathbf{b}) d\Omega - \int_{\Gamma_t} \delta\mathbf{u} \cdot \bar{\mathbf{t}} d\Gamma = 0 \tag{8}$$

$$\mathcal{L}_p = \int_\Omega (-\partial p \nabla \cdot \mathbf{u} : \boldsymbol{\sigma}' + \nabla \partial p \cdot \mathbf{q}_f)\, d\Omega = + \int_{\Gamma q} \delta p \cdot \bar{q} d\Gamma = 0 \tag{9}$$

2.2 | Spatial and temporal discretisation

In this study, the linear three-node triangular (T3) element is used for spatial discretisation of both the solid displacement $\mathbf{u}$ and the fluid pressure p. Thus the approximate compatible displacement and fluid pressure $\mathbf{u}^h$ and p^h could be obtained by Equations (10) and (11), where $\mathbf{U}$ is the nodal displacement vector and $\mathbf{P}$ is the nodal pore pressure vector. $\mathbf{N}^u$ and $\mathbf{N}^p$ are shape function matrices for $\mathbf{u}$ and p.

$$\mathbf{u}^h = \mathbf{N}^u \mathbf{U} \tag{10}$$

$$p^h = \mathbf{N}^p \mathbf{P} \tag{11}$$

Substituting interpolated displacement $\mathbf{u}^h$ and pore pressure p^h with their corresponding variations $\delta \mathbf{u}^h$ and δp^h into the equivalent weak forms shown in Equations (8) and (9), the coupled FEM equations—a system of time-dependent ordinary differential equations—are derived as:

$$\left\{ \begin{array}{l} L_u^h = \mathbf{F}^{\text{int}}(\mathbf{U}) - \mathbf{C}\mathbf{P} - \mathbf{F}^{\text{ext}} = 0 \\ L_p^h = -\mathbf{C}^T \mathbf{U} - \mathbf{K}^C, \mathbf{P} + \mathbf{Q} = 0 \end{array} \right\} \tag{12}$$

where the solid internal force $\mathbf{F}^{\text{int}}(\mathbf{U})$ is a nonlinear function of $\mathbf{U}$ due to elastoplasticity. Hydromechanical coupling matrix $\mathbf{C}$, permeability matrix $\mathbf{K}^c$, external force $\mathbf{F}^{\text{ext}}$ and flow flux $\mathbf{Q}^{\text{ext}}$ are presented in Equations (13)–(17). $\mathbf{m} = [\,1\ 1\ 0\,]^T$ is for plane strain problem, and $\mathbf{k}_f$ is the permeability coefficient matrix expressed by Equation (18). Compatible gradient matrices $\mathbf{B}^u$ and $\mathbf{B}^p$ are transformation matrix of gradient of $\mathbf{N}^u$ and $\mathbf{N}^p$ formulated in Equations (19) and (20). It can be easily derived that $\mathbf{B}^u$ and $\mathbf{B}^p$ are piecewise constants. n is the total number of nodes.

$$\mathbf{F}^{int}(\mathbf{U}) = \int_\Omega \mathbf{B}^{uT} \boldsymbol{\sigma}' d\Omega \tag{13}$$

$$\mathbf{K}^c = \int_\Omega \mathbf{B}^{pT} \mathbf{k}_f \mathbf{B}^p d\Omega \tag{14}$$

$$\mathbf{C} = \int_\Omega \mathbf{B}^{uT} \mathbf{m} \mathbf{N}^p d\Omega \tag{15}$$

$$\mathbf{F}^{\text{ext}} = \int_{\Gamma_t} \mathbf{N}^{uT} \bar{\mathbf{t}} d\Gamma + \int_\Omega \mathbf{N}^{uT} \mathbf{b} d\Omega \tag{16}$$

$$\mathbf{Q}^{\text{ext}} = \int_{\Gamma_q} \mathbf{N}^{pT} \bar{q} d\Gamma \tag{17}$$

$$\mathbf{k}_f = \frac{1}{\gamma_f} \begin{bmatrix} k_x & 0 \\ 0 & k_y \end{bmatrix} \tag{18}$$

$$\mathbf{B}^u = \mathbf{L}_d \mathbf{N}^u = \begin{bmatrix} \mathbf{B}_1^u & \mathbf{B}_2^u & \dots & \mathbf{B}_n^u \end{bmatrix}, \mathbf{L}_d = \begin{bmatrix} \frac{\partial}{\partial x} & 0 & \frac{\partial}{\partial y} \\ 0 & \frac{\partial}{\partial y} & \frac{\partial}{\partial x} \end{bmatrix}^T \tag{19}$$

$$\mathbf{B}^p = \mathbf{L}_f \mathbf{N}^p = \begin{bmatrix} \mathbf{B}_1^p & \mathbf{B}_2^p & \dots & \mathbf{B}_n^p \end{bmatrix}, \quad \mathbf{L}_f = \begin{bmatrix} \frac{\partial}{\partial x} & \frac{\partial}{\partial y} \end{bmatrix}^T \tag{20}$$

Finally, the temporal discretisation based on a trapezoidal rule[7,62] is adopted here. In the single time step from t_n to t_{n+1}, the pore pressure and flow flux are assumed to vary linearly, and the values at $t_{n+\theta}$ as in Equation (21) are taken to integrate the time-dependent mass conservation equation. Considering the residuals at t_{n+1}, the algebraic expression of hydromechanical coupled problem is stated as Equation (22). Unconditional temporal stability can be achieved if the integration parameter takes the value of $0.5 < \theta \leq 1$.[54,62] In this study, θ is fixed as 1, which implies a backward Euler method.

$$\begin{cases} \mathbf{P}_{t_{n+\theta}} = (1-\theta)\mathbf{P}_{t_n} + \theta\mathbf{P}_{t_{n+1}} \\ \mathbf{Q}^{\text{ext}}_{t_{n+\theta}} = (1-\theta)\mathbf{Q}^{\text{ext}}_{t_n} + \theta\mathbf{Q}^{ext}_{t_{n+1}} \end{cases} \tag{21}$$

$$\begin{pmatrix} \mathbf{R}_u \\ \mathbf{R}_p \end{pmatrix}_{n+1} = \begin{pmatrix} (\mathbf{F}^{ext})_{t_{n+1}} + \mathbf{C}\mathbf{P}_{t_{n+1}} - (\mathbf{F}^{int}(\mathbf{U}))_{t_{n+1}} \\ \mathbf{C}^T(\mathbf{U}_{t_{n+1}} - \mathbf{U}_{t_n}) + \Delta t\mathbf{K}^c\mathbf{P}_{t_{n+\theta}} - \Delta t\mathbf{Q}^{ext}_{t_{n+\theta}} \end{pmatrix} = \begin{pmatrix} \mathbf{0} \\ \mathbf{0} \end{pmatrix} \tag{22}$$

Noting that when the variation of geometry is prominent in one analysis step, the stress updating procedure should be conducted taking into account the spin tensor $\mathbf{w}$ and Jaumann rate, leading to Equations (23) and (24).

$$\boldsymbol{\sigma}^{k+1} = \boldsymbol{\sigma}^k + \Delta t(\mathbf{w}\cdot\boldsymbol{\sigma}^k - \boldsymbol{\sigma}^k\cdot\mathbf{w}) + \boldsymbol{D}_{ep} : \Delta\boldsymbol{\varepsilon}^k \tag{23}$$

$$\mathbf{W} = \frac{1}{2}(\nabla\dot{\mathbf{u}} - \nabla\dot{\mathbf{u}}^T) \tag{24}$$

The nonlinear residual equations are solved in the monolithic Newton–Raphson iterative framework, where the unknowns for the displacement and pore pressure are calculated simultaneously. The incremental solution for the $k+1$th iteration is determined as Equation (25), where $\mathbf{K}^m$ is the tangential stiffness matrix given by Equation (26). In this equation, the matrix $\mathbf{D}$ is denoted as the Voigt notation of the aforementioned D_{ep} in Equation (5).

$$\begin{bmatrix} \mathbf{K}^m & -\mathbf{C} \\ -\mathbf{C}^T & -\theta\Delta t\mathbf{K}^c \end{bmatrix}_k \begin{bmatrix} \Delta\mathbf{U} \\ \Delta\mathbf{P} \end{bmatrix}_{(k+1)} = \begin{bmatrix} \mathbf{R}_u \\ \mathbf{R}_p \end{bmatrix}_k \tag{25}$$

$$\mathbf{K}^m = \int_\Omega \mathbf{B}^{uT}\mathbf{D}\mathbf{B}^u d\Omega \tag{26}$$

2.3 | Smoothing technique and stable nodal integration

Comparing with FEM-T3, the advantages of the node-based smoothed FEM (NS-FEM) include insensitivity to mesh distortion, more accurate in strain energy norm and ease of volumetric locking.[33] Moreover, it could be easily improved to the particle-type method NS-PFEM for large deformation analysis, because all quantities of interest are directly stored and updated based on the nodes, and the variable mapping from the quadrature points could be avoided.

It should be noted that NS-FEM has great potential but is not always locking-free when treating the nearly incompressible solids.[34] Only when the number of nodes is large enough and the ratio r of the number of unknown degrees of freedom (DOF) and incompressible constraints approaches the optimal value 2,[13,34] the results of NS-FEM will approach the locking-free mode. In view of this, some potential remedies have been considered when using NS-FEM in the nearly incompressible limit, such as the dual mesh,[63] PPP[35] and selective integration scheme.[64] Such techniques can also be applied in the SNS-PFEM to overcome the volumetric locking problem. In this paper for hydromechanical modelling, only the compressible solids with the Poisson's ratio smaller than 0.4 as soils are simulated.

The code of NS-FEM can be constructed based on an FEM-T3 code by several major modifications. Although it is more complicated than adding a new element into an existing FEM code, the conversion of a traditional FEM code into an NS-FEM code is still relatively simple. The first step is to construct the smoothing domain. A node-based smoothing domain Ω^s_k marked by the node with position $\mathbf{x}_k$ is composed of several subdomains $\Omega^s_{k,q}$, whose vertexes are the centroid of the element and two midpoints of edge, as Figure 1 shows. Then, the gradient smoothing technique is presented based on the weighting function (using piecewise constant shown in this study as Equation 27) and smoothing operation in Equation (28). In a specific node-based smoothing domain Ω^s_k, the strain is assumed to be smoothed as a constant by Equation (29).

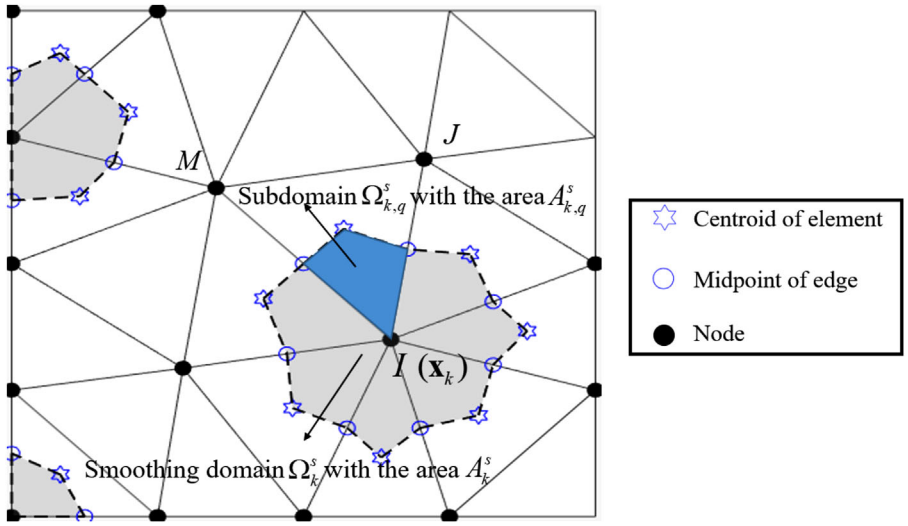

FIGURE 1 Schematic of the construction of node-based smoothing domain

By using the smoothed strain $\bar{\boldsymbol{\varepsilon}}$ with constitutive rules, the smoothed stress field $\bar{\boldsymbol{\sigma}}$ could be calculated. Accordingly, the smoothed gradient matrices $\bar{\mathbf{B}}_I^u, \bar{\mathbf{B}}_I^p$ can then be derived by the smoothing operation as in Equations (30) and (31) from the original compatible gradient matrices $\mathbf{B}_I^u, \mathbf{B}_I^p$ in Equations (19) and (20). In Equation (27)–(31), A_k^s is the area of smoothing domain Ω_k^s and $A_{k,q}^s$ is the area of subdomain $\Omega_{k,q}^s$.

$$W(\mathbf{x}_k - \mathbf{x}) = \begin{cases} 1/A_k^s, \mathbf{x} \in \bar{\Omega}_k^s \\ 0, \mathbf{x} \notin \bar{\Omega}_k^s \end{cases} \tag{27}$$

$$\bar{\nabla} N_I(\mathbf{x}) = \int_{\Omega_k^s} \nabla N_I(\mathbf{x}) W(\mathbf{x}_k - \mathbf{x}) d\mathbf{x} \tag{28}$$

$$\bar{\boldsymbol{\varepsilon}}(\mathbf{x})|_{\Omega_k^s} = \frac{1}{A_k^s} \int_{\Omega_k^s} \boldsymbol{\varepsilon}(\mathbf{x}) d\Omega \tag{29}$$

$$\bar{\mathbf{B}}_I^u(\mathbf{x}) = \int_{\Omega_k^s} \mathbf{B}_I^u(\mathbf{x}) W(\mathbf{x}_k - \mathbf{x}) d\mathbf{x} = \frac{1}{A_k^s} \sum_{q=1}^{n_k} A_{k,q}^s \mathbf{B}_{I,q}^u, \forall \mathbf{x} \in \bar{\Omega}_k^s \tag{30}$$

$$\bar{\mathbf{B}}_I^p(\mathbf{x}) = \int_{\Omega_k^s} \mathbf{B}_I^p(\mathbf{x}) W(\mathbf{x}_k - \mathbf{x}) d\mathbf{x} = \frac{1}{A_k^s} \sum_{q=1}^{n_k} A_{k,q}^s \mathbf{B}_{I,q}^p, \forall \mathbf{x} \in \bar{\Omega}_k^s \tag{31}$$

The smoothed Galerkin weak form is presented in Equation (38), where the smoothed internal force $\bar{\mathbf{F}}^{int}(\mathbf{U})$, smoothed hydromechanical coupling matrix $\bar{\mathbf{C}}$ and smoothed permeability matrix $\bar{\mathbf{K}}^c$ are obtained by replacing the compatible gradients in Equations (13)–(15) with the smoothed counterparts of Equations (29)–(31). The smoothed stiffness matrix $\bar{\mathbf{K}}^m$ is formulated in the same way.

$$\left\{ \begin{array}{l} \bar{\mathcal{L}}_{u^h} = \bar{\mathbf{F}}, (\mathbf{U}) - \bar{\mathbf{C}} P - \mathbf{F}^{ext} = 0 \\ \bar{\mathcal{L}} u^h = \bar{\mathbf{C}}^T \dot{\mathbf{U}} - \bar{\mathbf{K}}^c \mathbf{P} + \mathbf{Q}^{ext} = 0 \end{array} \right\} \tag{32}$$

$$\begin{bmatrix} \bar{\mathbf{K}}^m & -\bar{\mathbf{C}} \\ -\bar{\mathbf{C}}^T & -\theta \Delta t \bar{\mathbf{K}}^c \end{bmatrix}_k \begin{bmatrix} \Delta \mathbf{U} \\ \Delta \mathbf{P} \end{bmatrix}_{(k+1)} = \begin{bmatrix} \mathbf{R}_u \\ \mathbf{R}_p \end{bmatrix}_k \tag{33}$$

The stiffness, permeability and coupling matrices could be assembled with direct NI, which only use the smoothed gradients of shape functions. However, the singular mode intrinsically caused by NI must be focused on owing to the violation of integration constraints,[45,65,66] which could be clearly caught in many meshfree and S-FEM simulations.[19,39] In the example 3.3 of this study, the spurious spatial oscillations could be observed in the contours of displacement, stress

and pore pressure when direct NI is applied. Puso et al. (2008) developed a modified stabilised conforming nodal integration (MSCNI) method to correct this error[30,31] and applied it in meshfree hydromechanical analysis.[19] With MSCNI, each integration domain is divided to several subdomains, each of which is assigned with a stress stabilisation point. The smoothed shape function gradient of stabilisation points is calculated based on the subdomain to eliminate the integration oscillation.

In this numerical framework, a stabilisation technique similar to MSCNI is developed to reach a NS-PFEM with stabilised NI (SNS-PFEM). The primary difference in coding is that in a meshfree interpolation scheme, such as reproducing kernel particle or element-free Galerkin method, extra evaluation of smoothed gradient at each additional stress point is unavoidable. However, due to the linear shape function and its piecewise constant derivatives in NS-PFEM, these counterparts just take the same value as the compatible gradient matrices that have been calculated beforehand, so that no extra computational effort is required. The stabilisation technique first introduces some additional terms into Equation (32) to formulate the stabilised smoothed weak form in Equations (34) and (35), where the $\Delta\mathbf{u}$and Δp are incremental displacement and pore pressure separately at the current calculation step. Then it leads to the modified formulations of smoothed stiffness, permeability and coupling matrices in SNS-PFEM as Equations (36)–(38) by linearisation. The integration stabilisation coefficient ε_s is fixed as 1 by default in all the simulations of this study, as suggested in related papers.[19,30] This coefficient ε_s could also be altered to achieve better balance between the accuracy and numerical stability if necessary.[30] $\varepsilon_s = 0$ signifies a retreat to the NS-PFEM.

$$\bar{\mathcal{L}}_u^h = \left(\int_\Omega \bar{\mathbf{B}}^{uT}\bar{\boldsymbol{\sigma}}d\Omega + \varepsilon_s\int_\Omega (\bar{\mathbf{B}}^u - \mathbf{B}^u)^T\mathbf{D}(\bar{\mathbf{B}}^u - \mathbf{B}^u)\Delta\mathbf{u}d\Omega\right) - \left(\int_\Omega \bar{\mathbf{B}}^{uT}\mathbf{m}\mathbf{N}^p d\Omega\right)\mathbf{P} - \mathbf{F}^{ext} = 0 \tag{34}$$

$$\bar{\mathcal{L}}_p^h = -\left(\int_\Omega \bar{\mathbf{B}}^{uT}\mathbf{m}\mathbf{N}^p d\Omega\right)^T \mathrm{d}\mathbf{U} - \left(\left(\int_\Omega \bar{\mathbf{B}}^{pT}\mathbf{k}_f\bar{\mathbf{B}}^p d\Omega\right)\mathbf{P} + \varepsilon_s\int_\Omega (\bar{\mathbf{B}}^p - \mathbf{B}^p)^T\mathbf{k}_f(\bar{\mathbf{B}}^p - \mathbf{B}^p)\Delta p d\Omega\right) + \mathbf{Q}^{ext} = 0 \tag{35}$$

$$\begin{aligned}[\bar{\mathbf{K}}_{IJ}^m]_{\Omega_k^s} &= \int_{\Omega_k^s}\bar{\mathbf{B}}_I^{uT}\mathbf{D}\bar{\mathbf{B}}_J^u d\mathbf{x} + \varepsilon_s\sum_{q=1}^{n_k}\int_{\Omega_{k,q}^s}(\bar{\mathbf{B}}_I^u - \mathbf{B}_I^u)^T\mathbf{D}(\bar{\mathbf{B}}_J^u - \mathbf{B}_J^u)d\mathbf{x}\\ &= \bar{\mathbf{B}}_I^{uT}|_{\Omega_k^s}\mathbf{D}\bar{\mathbf{B}}_J^u|_{\Omega_k^s}A_k^s + \varepsilon_s\sum_{q=1}^{n_k}(\bar{\mathbf{B}}_I^u|_{\Omega_{k,q}^s} - \mathbf{B}_I^u|_{\Omega_{k,q}^s})^T\mathbf{D}(\bar{\mathbf{B}}_J^u|_{\Omega_{k,q}^s} - \mathbf{B}_J^u|_{\Omega_{k,q}^s})A_{k,q}^s\end{aligned} \tag{36}$$

$$\begin{aligned}[\bar{\mathbf{K}}_{IJ}^c]_{\Omega_k^s} &= \int_{\Omega_k^s}\bar{\mathbf{B}}_I^{pT}\mathbf{k}_f\bar{\mathbf{B}}_J^p d\mathbf{x} + \varepsilon_s\sum_{q=1}^{n_k}\int_{\Omega_{k,q}^s}(\bar{\mathbf{B}}_I^p - \mathbf{B}_I^p)^T\mathbf{k}_f(\bar{\mathbf{B}}_J^p - \mathbf{B}_J^p)d\mathbf{x}\\ &= \bar{\mathbf{B}}_I^{pT}|_{\Omega_k^s}\mathbf{k}_f\bar{\mathbf{B}}_J^p|_{\Omega_k^s}A_k^s + \varepsilon_s\sum_{q=1}^{n_k}(\bar{\mathbf{B}}_I^p|_{\Omega_{k,q}^s} - \mathbf{B}_I^p|_{\Omega_{k,q}^s})^T\mathbf{k}_f(\bar{\mathbf{B}}_J^p|_{\Omega_{k,q}^s} - \mathbf{B}_J^p|_{\Omega_{k,q}^s})A_{k,q}^s\end{aligned} \tag{37}$$

$$[\bar{\mathbf{C}}_{IJ}]_{\Omega_k^s} = \int_{\Omega_k^s}\bar{\mathbf{B}}_I^{uT}\mathbf{m}\mathbf{N}^p d\mathbf{x} \tag{38}$$

The integration shown in Equation (38) could be reformulated as the multiplication of a constant B matrix with a integration of linear shape function in each subdomain $\Omega_{k,q}^s$, whereas the latter could be conducted analytically as in Equation (39), where the relative position of nodes I, J and M are marked in Figure 1. Thus, all stable NI shown in Equations (36)–(38) can be conducted by the weighted sum of subdomain area, which minimises the computational cost due

to inner loop on the quadrature points.

$$\int_{\Omega_{k,q}^s} N_L d\mathbf{x} = \begin{cases} \frac{11}{18} A_{k,q}^s, \text{if} L = I \\ \frac{7}{36} A_{k,q}^s, \text{if} L \in \{J, M\} \\ 0, \text{otherwise} \end{cases} \tag{39}$$

2.4 | Polynomial pressure projection (PPP)

There is an inherent numerical defect for hydromechanical coupled simulation when low-order interpolations are equally adopted for displacement and pressure field. In the undrained limit, that is, low permeability with very short time, non-physical pore pressure oscillations appear if the interpolants are not adequately selected or other numerical techniques to alleviate such numerical pathology are not employed, as exhibited in many numerical methods including the FEM,[54] RKPM[45] and MPM.[52] A conceptual insight can be obtained by considering the four-block structure of the coefficient matrix in Equation (33). In the undrained limit when the p–p block approaches zero, solvability and stability of the algebraic formulation as Equation (40) requires some extra necessary conditions.[53,67] The most important one is the discrete inf-sup LBB condition for the interpolation spaces S_u^h and S_p^h as in Equation (41), where C_0 is a positive constant independent of the features of spatial discretisation, that is, the element size. In mixed u–p FEM, specially designed Taylor–Hood element pairs are widely used to meet the LBB condition when solving nearly incompressible problems.[57]

$$\begin{bmatrix} \bar{\mathbf{K}}^m & -\bar{\mathbf{C}} \\ -\bar{\mathbf{C}}^T & 0 \end{bmatrix} \begin{bmatrix} \Delta \mathbf{U} \\ \Delta \mathbf{P} \end{bmatrix} = \begin{bmatrix} \mathbf{R}_u \\ \mathbf{R}_p \end{bmatrix} \tag{40}$$

$$\sup_{\mathbf{u}^h \in S_u^h} \frac{\int_\Omega p^h \nabla \cdot \mathbf{u}^h d\mathbf{x}}{\|\mathbf{u}^h\|_1} \geq C_0 \|p^h\|_0, \forall p^h \in S_p^h \tag{41}$$

$$\sup_{\mathbf{u}^h \in S_u^h} \frac{\int_\Omega p^h \nabla \cdot \mathbf{u}^h d\mathbf{x}}{\|\mathbf{u}^h\|_1} \geq C_1 \|p^h\|_0 - \sum_{\Omega_e} C_2 \left\| p^h - \prod p^h \right\|_0, \forall p^h \in S_p^h \tag{42}$$

$$\prod p^h(\mathbf{x})|_{\Omega_e} = \frac{1}{V_e} \int_{\Omega_e} p^h(\mathbf{x}) d\mathbf{x} \tag{43}$$

Undoubtedly, the equal-order T3 interpolation of $\mathbf{u}$ and p used in the SNS-PFEM has been proved to violate the LBB condition in Equation (41).[68] It is necessary to find a stabilisation scheme which can overcome the spurious pressure oscillation in undrained limit and also preserve the accuracy in drained conditions. Fortunately, Bochev et al.[61] discovered that the linear-order element pair satisfies a weak inf-sup condition in Equation (42), where C_1 and C_2 are positive constants independent of discretisation. Here in Equation (42), the L_2 projection operator $\prod$ that maps the pore pressure field into a lower-order polynomial space needs to be identified. The operator is determined as the one that minimises the functional $\|p^h - \prod p^h\|_{L_2(\Omega_e)}^2$, where Ω_e is the element domain of S_p^h in T3 interpolation. Then it could be concluded that the operator $\prod$ is the element-average projection defined in Equation (43). Based on the weak inf-sup condition Equation (42), the idea of PPP is proposed to compensate the deficiency of LBB condition of interpolation space pair by adding a stabilisation term into the equivalent weak form, as in Equation (44). Detailed derivations can be found in previous studies.[53,67,69]

$$\bar{\mathcal{L}}_{p,stab}^h = \bar{\mathcal{L}}_p^h - \int_\Omega \varepsilon_f \left[\delta p^h - \prod \delta p^h \right] \frac{\partial}{\partial t} \left[p^h - \prod p^h \right] d\mathbf{x} = 0 \tag{44}$$

$$\left(\begin{bmatrix} \bar{\mathbf{K}}^m & -\bar{\mathbf{C}} \\ -\bar{\mathbf{C}}^T & -\theta \Delta t \bar{\mathbf{K}}^c \end{bmatrix}_k - \begin{bmatrix} 0 & 0 \\ 0 & \mathbf{S} \end{bmatrix}_k \right) \begin{bmatrix} \Delta \mathbf{U} \\ \Delta \mathbf{P} \end{bmatrix}_{(k+1)} = \begin{bmatrix} \mathbf{R}_u \\ \mathbf{R}_p \end{bmatrix}_k + \begin{bmatrix} 0 \\ \mathbf{H}_{t_{n+1}}^{stab} \end{bmatrix}_k \tag{45}$$

$$\mathbf{S} = \int_\Omega \varepsilon_f \left[\mathbf{N}^p - \prod \mathbf{N}^p \right]^T \left[\mathbf{N}^p - \prod \mathbf{N}^p \right] d\mathbf{x} \tag{46}$$

$$\mathbf{H}_{t_{n+1}}^{\text{stab}} = \int_{\Omega} \varepsilon_f \left[\mathbf{N}^p - \prod \mathbf{N}^p\right]^T \left[\left(p^h - \prod p^h\right)_{t_{n+1}} - \left(p^h - \prod p^h\right)_{t_n}\right] d\mathbf{x} \tag{47}$$

In this study, a stabilisation term of PPP is formulated in SNS-PFEM to reach a modified variational equation of continuity as in Equation (44), which is similar to what White and Borja used in Q4-P4 elements.[54,70] Moreover, an automatic estimation technique of stabilisation parameter ε_f proposed by Sun et al.[69] is adopted, which considers the compressibility of fluid and solid grains, and the variation of time step and mesh size,[69,71] as in Equations (48)–(51):

$$\varepsilon_f = \frac{1}{M'} \left\langle 1 - 3\frac{c_w \Delta t}{h^2} \right\rangle \left(1 + \tanh\left(2 - 12\frac{c_w \Delta t}{h^2}\right)\right) \tag{48}$$

$$c_w = k_f M' \tag{49}$$

$$M' = \frac{K + 4G/3}{(K + 4G/3)/M_B + 1} \tag{50}$$

$$M_B = \frac{K_s K_f}{\left[K_f(1 - n_f) + K_s n_f\right]} \tag{51}$$

where Δt is the current length of time step,K_s the bulk modulus of solid grains, K_f the bulk modulus of fluid, $K$and G the bulk and shear modulus of solid skeleton separately and n_f is the porosity of solid. h is a characteristic length of spatial discretisation, which is evaluated by $h = \sqrt{A_k^s}$ for each smoothing domain. Here, the K_s= 50 GPa and K_f = 2 GPa are fixed as a weak-compressibility approximation of the mixture to estimate the stabilisation parameter, seeing in Sun et al.[69] According to Equation (50), the constrained modulus M' is very close to $K + 4G/3$ as long as the K_s and K_f are set much larger than the solid skeleton modulus K and G. All the parameters used here are either material properties or discretisation sizes decided by the numerical model, and no calibration is needed. As the time step and permeability grow from extremely low to relatively high levels, the ε_f will decrease to zero gradually. With these formulations, the PPP can preserve both accuracy and stability from undrained limit to drained conditions.[67,72]

In solving the stabilised equations of smoothed Galerkin weak form, the modified Newton–Raphson iterative formulations can be written as Equations (45)–(47). Only a stabilisation block $\mathbf{S}$ and a stabilisation residual $\mathbf{H}_{t_{n+1}}^{\text{stab}}$ need to be formulated to modify the iteration format, leaving all the remaining procedures unchanged. This is an obvious advantage of PPP, whereby adding only some minor plug-ins to the original SNS-PFEM code could achieve a prominent stability effect.

As indicated in Equations (42), (44) and (45), the stabilisation term is only related to the element-based shape function and projection operator of interpolated pressure space, free of using the gradients of shape function. Therefore, the smoothing operation is not applied in the sub block $\mathbf{S}$. For the consistency of code, the assembly of block $\mathbf{S}$ could still be reformulated to an NI procedure as shown in Equations (52) and (53). It arises from the fact that the value of $\mathbf{S}$ for each T3 element is nothing more than a constant matrix scaled by its area. So, it can be evenly distributed to the three subdomains. Now, all the subblocks in Equation (45) are integrated without any quadrature points. These analytical formulations as in Equations (39) and (52) not only offer considerable CPU time saving and high accuracy but also reduce the numerical risk from distorted mesh, since the evaluation of Jacobian determinant is avoided.

$$[\mathbf{S}]_{\Omega_{k,q}^s} := \varepsilon_f \mathbf{H}_f A_{k,q}^s \tag{52}$$

$$\mathbf{H}_f = \begin{bmatrix} a & b & b \\ b & a & b \\ b & b & a \end{bmatrix}, \text{with} a = \frac{1}{18} \text{and} b = -\frac{1}{36} \tag{53}$$

2.5 | Re-meshing strategy for large deformation simulation

In large deformation analysis, if the initial configuration and mesh are kept constant, serious errors will occur because the small strain assumption no longer holds when there is sufficiently large deformation gradient. The traditional method of mesh updating based on pure displacement increment is always accompanied with mesh entanglement. In PFEM, a novel strategy is developed using particle discretisation strategy.[5,73–76] Particles with updated positions are regarded as the cloud for domain discretisation, whose connectivity are renewed via Delaunay triangulation in each remeshing step to reduce the mesh distortion. The alpha shape technique is applied to delete unreasonable elements on boundary.[74] As long as the mesh has been updated, the subsequent calculation in the current step is just the same as regular NS-FEM. Comparing with traditional PFEM or ES-PFEM, NS-PFEM has the advantage of high accuracy. Since all physical quantities of interest are stored at nodes (i.e., displacements, pore pressure) or updated by the node-based smoothing domains (i.e., strain, stress, state variables of soil model), variable mapping between the nodes and quadrature points is not needed, resulting in the reduction of accuracy loss. Because the total variation of geometry has been decomposed into a number of small incremental sub steps, the accuracy of infinitesimal strain formulation with Cauchy stress shown in Equations (4) and (5) could still be preserved, which is also widely adopted and verified in previous PFEM-based large deformation simulations.[74,77,78]

3 | VERIFICATION OF THE NUMERICAL APPROACH

Four benchmark hydromechanical coupled problems are simulated using the proposed SNS-PFEM. Analytical solutions of the 1-D Terzaghi consolidation and Mandel's model under normal compression are available to validate our numerical results.[5,19,52,79,80] When dealing with Mandel's model under shear force and strip footing consolidation with Mohr–Coulomb (MC) soil, several reliable numerical solutions are provided as references.[8,37,39,81] The vertical cut problem is also simulated by the proposed SNS-PFEM with PPP to investigate the evolution of local failure. The effectiveness of PPP and NI stabilisation is discussed by simulating the same case with these techniques activated or not. Besides, the performance of SNS-PFEM is also compared with other reliable numerical results which use different numerical methods or stabilisation techniques.[39,82]

3.1 | 1D Terzaghi's consolidation

Terzaghi's 1-D model of consolidation in saturated elastic soil[80] has been a primary validation test for most newly developed coupled numerical methods.[5,19,37,39,52,54,62,82] In this study, a porous rectangular medium of 1 m drainage height and 0.06 m width is taken, with the lateral displacement of left and right edge, and both directions of the bottom edge are fixed, as shown in Figure 2. Only the top surface is permeable. A uniform mesh with 255 nodes and 402 elements is used. The elastic parameters are set as Young's modulus $E = 10$ MPa, Poisson's ratio $\nu = 0.3$. The unit weight of fluid is $\gamma_w = 10\ \mathrm{kN/m^3}$.

A uniform load of $P_0 = 10$ kPa is applied on the drainage surface instantly at the first time step. The dimensionless time is defined as in Equation (54). Two different cases 1 and 2 are investigated. For case 1 exhibited in Figures 3 and 4A, the total period of $t = 5$ s, the time step of $\Delta t = 1$ s and the permeability of $k = 10^{-9}$ m/s are set to approach the undrained limit which tends to trigger the pressure oscillation mode. This parameter setting also agrees with the same example analysed in a recent study.[39] For case 2 shown Figure 4B, another setting of $t = 15$ s, $\Delta t = 0.02$ s and $k = 10^{-4}$ m/s is adopted which is corresponding to the drained conditions. The value of PPP parameter ε_f is determined by the Equation (48).

$$T = \frac{c_v t}{H^2}, \text{with } c_v = \frac{k}{m_v \gamma_w},\ m_v = \frac{(1+\nu)(1-2\nu)}{E(1-\nu)} \tag{54}$$

As Figure 3A shows, in case 1 if the pressure stabilisation coefficient ε_f and integration stabilisation coefficient ε_s both take the value 0, the severe fluid pressure oscillation in the undrained limit could be captured. $\varepsilon_s = 1$ with $\varepsilon_f = 0$ leads to some stabilisation as in Figure 3B, whereas $\varepsilon_s = 0$ with PPP would produce a much more significant effect in Figure 3C. A combination of both stabilisation remedies taking $\varepsilon_s = 1$ and PPP will eliminate this instability and generate a result in good agreement with the analytical solution. It can be concluded that PPP solves the problem of spurious pressure oscillations effectively, although NI stabilisation could also help somewhat. This conclusion can also be supported by a related study,[39] in which the newly developed I-NSPIM and I-NSRPIM based on only the NI stabilisation

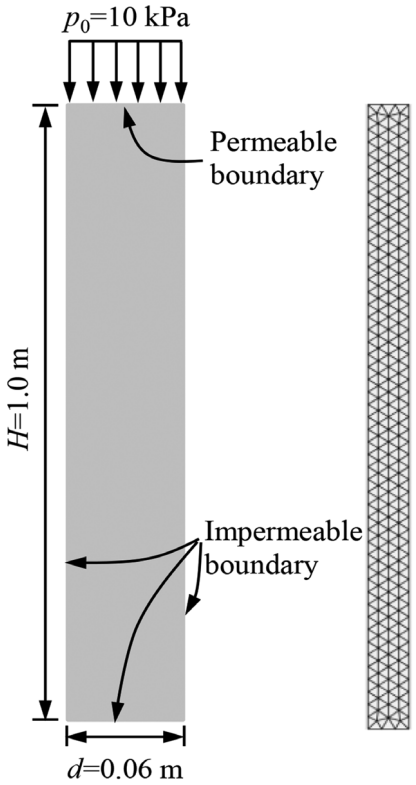

FIGURE 2 1-D Terzaghi consolidation with mesh

FIGURE 3 Distribution of normalised pore pressure with normalised depth in the undrained limit (case 1) with different numerical settings: (A) $\varepsilon_s = 0$, $\varepsilon_f = 0$; (B) $\varepsilon_s = 1$, $\varepsilon_f = 0$; (C) $\varepsilon_s = 0$, $\varepsilon_f = 1.47 \times 10^{-4}$; (D) $\varepsilon_s = 1$, $\varepsilon_f = 1.47 \times 10^{-4}$

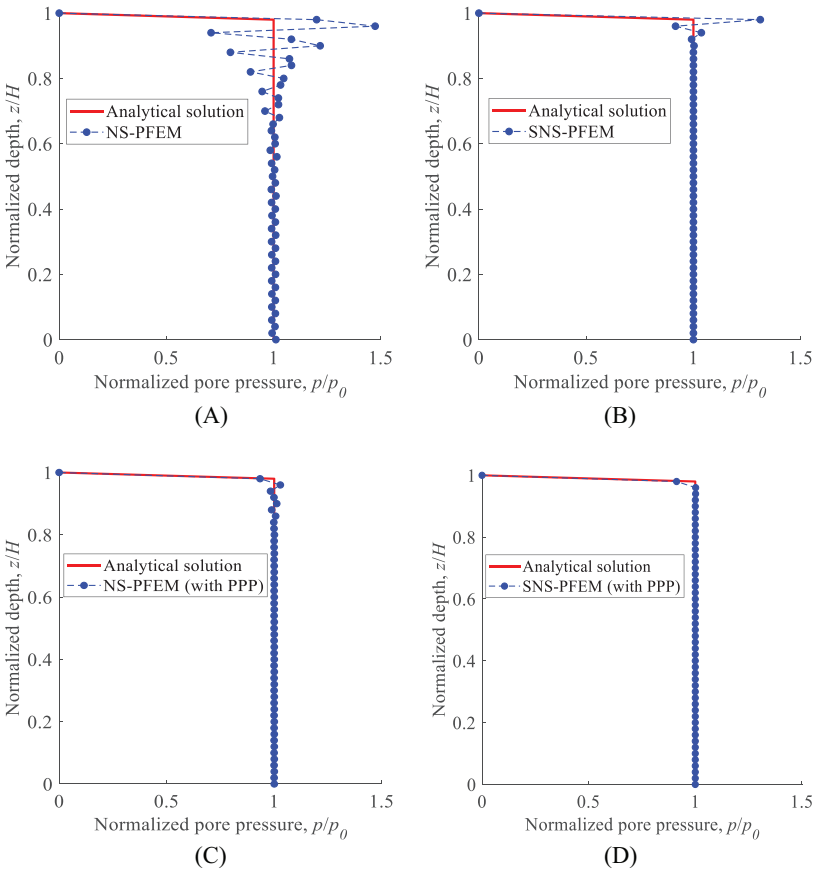

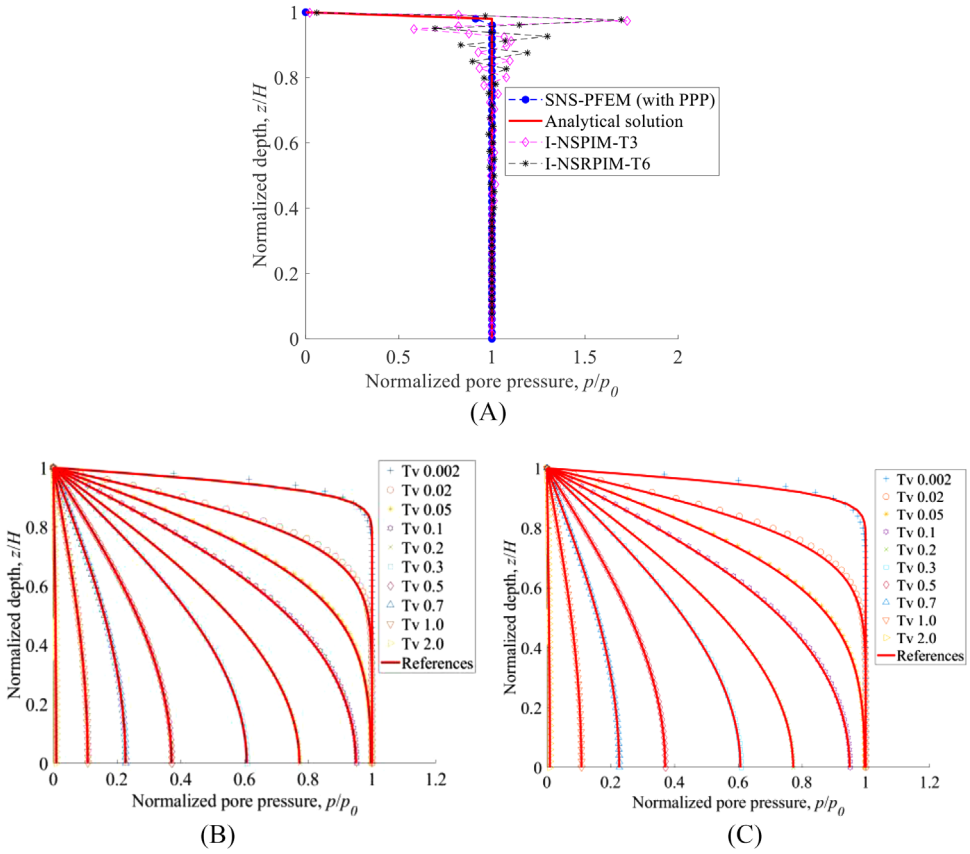

FIGURE 4 (A) Comparison of SNS-PFEM + PPP with other stabilisation methods[39] (case 1); (B) 1-D Terzaghi consolidation with SNS-PFEM ($\varepsilon_f = 0$) in drained condition (case 2); (C) 1-D Terzaghi consolidation with SNS-PFEM + PPP ($\varepsilon_f = 1.39 \times 10^{-4}$) in drained condition (case 2). PPP, polynomial pressure projection; SNS-PFEM, stabilized node-based smoothed particle finite element method

strategy[46–49] are adopted. As Figure 4A shows, their effect is limited, indicating that pure NI modification cannot totally stabilise the pore pressure. Figure 4B, C presents that in case 2, the results are reasonable with both $\varepsilon_f = 0$ and ε_f in Equation (48). PPP is unnecessary in the drained condition, because the permeability and drainage period are large enough to avoid triggering the numerical instability. But it does not introduce any additional error since the stabilisation parameter can be reduced to a reasonable level (i.e., approaching zero) as the permeability increases. The foregoing results demonstrate that the PPP is highly efficient in overcoming the pore pressure oscillation in the SNS-PFEM framework, especially in conditions of low permeability and short period, with integration stabilisation techniques also able to help somewhat. Besides, PPP performs well in the drained problems with the automatic stabilisation calibration scheme.

3.2 | Mandel's problem

As Figure 5 shows, a sandwich-like saturated elastic soil subjected to an instant external load on the top is investigated, where the left and right sides are set as drainage boundaries. The classical theory about the Mandel–Cryer effect states that for the normal compression model in Figure 5A, the excess pore water pressure at the centre point A will evolve in a nonmonotonic manner, first increasing and then decreasing.[79] Later studies revealed that replacing the normal compression with shear force could lead to a similar effect[82,83] but one that is more sophisticated and that poses a greater challenge to numerical simulation.[39]

Here, the SNS-PFEM is implemented in both the normal compression and shear modes, aiming to reproduce the Mandel–Cryer effect. A uniform mesh with 845 nodes and 1560 elements is adopted. The parameters are the same as in the recent study[39] to ensure a fair comparison: Young's modulus $E = 100$ MPa, Poisson's ratio $\nu = 0.2$, unit weight of fluid $\gamma_w = 10$ kN/m^3, permeability $k = 10^{-4}$ m/s, the total period of $t = 300$ s and time step of $\Delta t = 0.05$ s. A uniform load

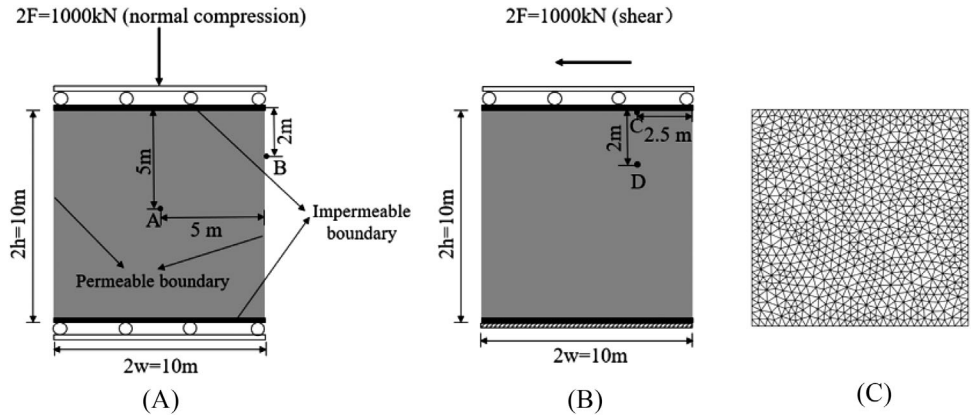

FIGURE 5 Mandel's problem: (A) normal compression mode; (B) shear force mode; (C) mesh

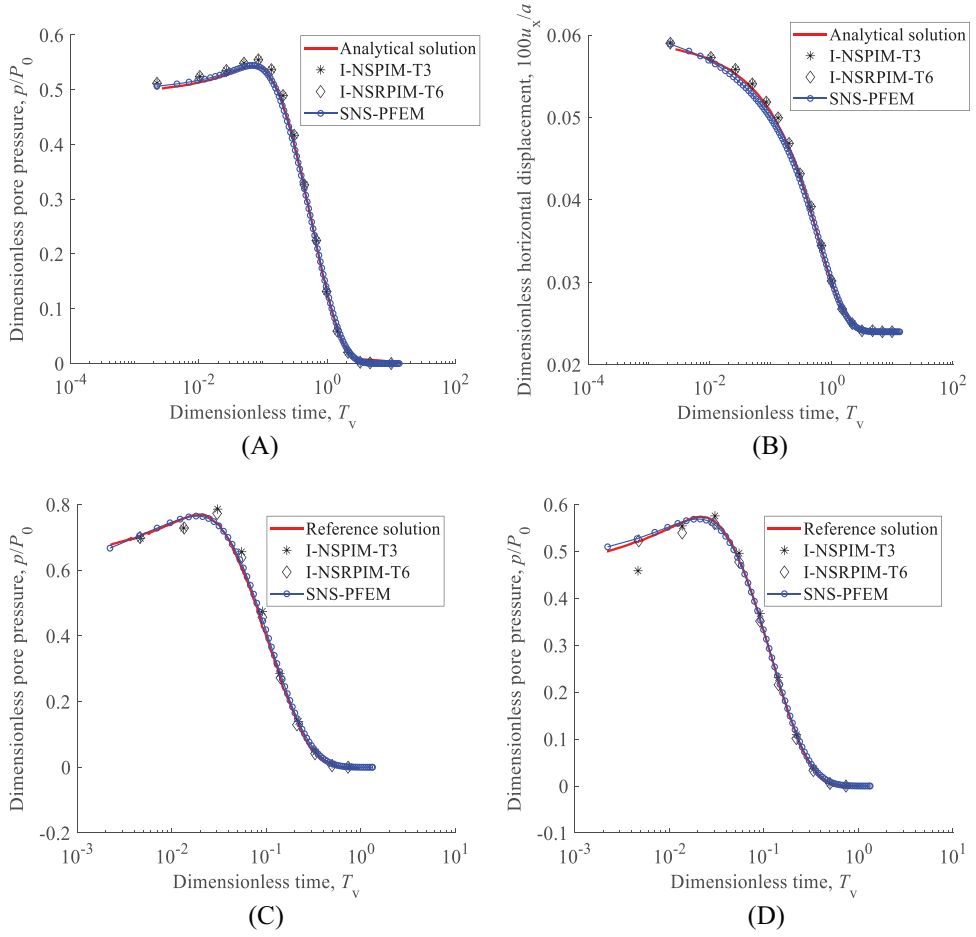

FIGURE 6 Evolution of (A) dimensionless pore pressure at point A; (B) dimensionless horizontal displacement at point B; (C) dimensionless pore pressure at point C and (D) dimensionless pore pressure at point D by different numerical methods

of $P_0 = 100$ kPa is applied on the top instantly in the first time step vertically or laterally for two modes. The pore pressure stabilisation is activated. Four watch points A, B, C and D are set as shown in Figure 5 to output the variables of interest. Results and comparisons are recorded in Figure 6. The definition of dimensionless time for this problem is defined the same as in Equation (54), where H takes the value of half hight h in Figure 5A.

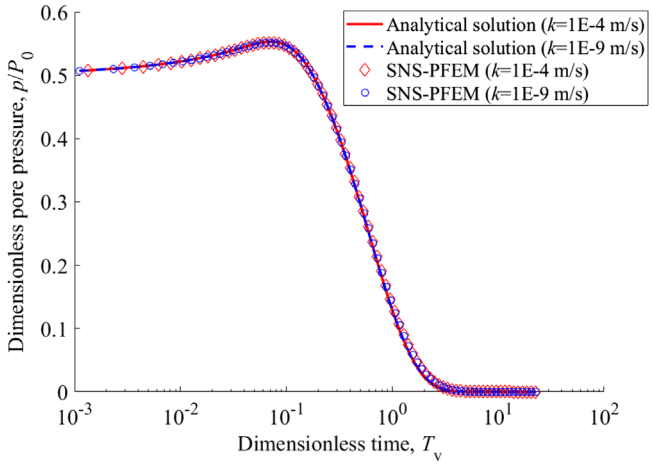

FIGURE 7 Evolution of dimensionless pore pressure at point A with different permeabilities

From Figure 6, all the curves of pore pressure and displacement accord well with the analytical solutions[82] or reference solutions.[39] For the normal compression mode, pore pressure at A goes up first, then down, as predicted by Mandel–Cryer effect and seen in Figure 6A. The horizontal position of the right edge expands instantly then gradually shrinks until drainage consolidation is finished, as shown in Figure 6B. Pore pressure at points C and D in the shear mode evolves similarly, as shown in Figure 6C, D, where the reference solution is provided by an FEM simulation with very fine mesh.[39] SNS-PFEM performance is better than that of I-NSPIM and I-NSRPIM in ref.[39] at early stage, as indicated in Figure 6C, D. In summary, the proposed SNS-PFEM with PPP reproduces the Mandel–Cryer effect well for both normal compression and shear mode, with its greater accuracy comparable to the recently proposed I-NSPIM and I-NSRPIM. Figure 7 presents the results of normal compression mode with different permeabilities. The length of dimensionless time is set as the same in different cases for comparison. The results shows that the performance of SNS-PFEM with PPP is quite good to exhibit the Mandel–Cryer effect clearly even under a very low permeability $k = 10^{-9}$ m/s.

3.3 | Strip footing consolidation of Mohr–Coulomb soil

The simulation of long-term consolidation is implemented in MC soil under a flexible footing load to assess the performance of coupled SNS-PFEM with material nonlinearity. A discretised half configuration considering the symmetry with load and boundary condition is exhibited in Figure 8, where the half width of footing is $a = 3$ m. A nonuniform mesh of 580 nodes and 1071 elements is adopted. A distorted mesh by randomly shifting the position of nodes is also presented to check the robustness of SNS-PFEM under the biased spatial discretisation. The top surface is free-draining except the segment under the bottom of footing which is impermeable. The material parameters for MC model are listed as follows: Young's modulus $E = 2000$ kPa, Poisson's ratio $\nu = 0.3$, friction angle $\phi = 20°$, dilatancy angle $\psi = 20°$ and cohesion $c = 10$ kPa. The permeability is set to $k = 10^{-5}$ m/day. The unit weight of fluid is $\gamma_w = 10$ kN/m^3. The dimensionless time in

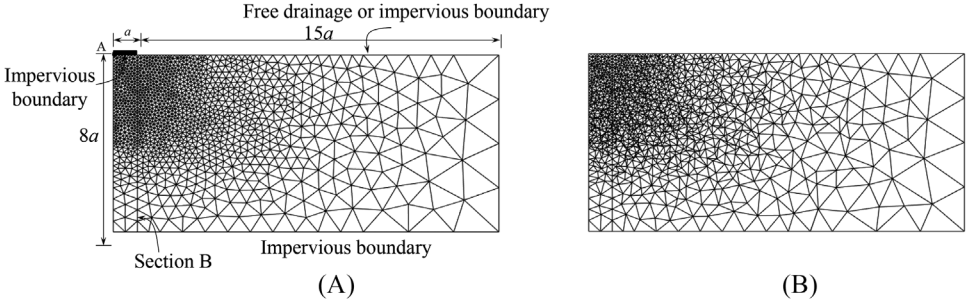

FIGURE 8 Geometry and mesh of strip footing consolidation: (A) regular mesh; (B) distorted mesh

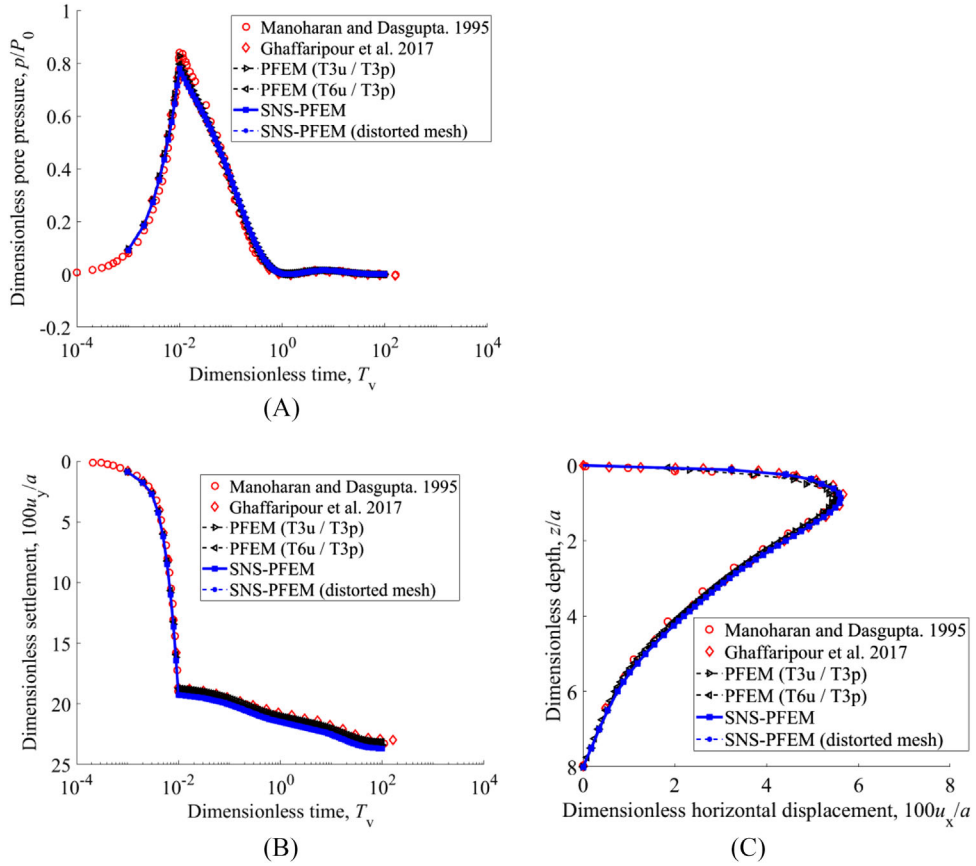

FIGURE 9 (A) Evolution of dimensionless pore pressure at point A; (B) evolution of dimensionless vertical displacement at point A; (C) distribution of dimensionless horizontal displacement with dimensionless depth along the section B with different numerical methods or spatial discretisation

this plane strain problem is defined as $T_v = \frac{Ekt}{2\gamma_w(1+\nu)(1-2\nu)a^2}$. $P_0 = 100$ kPa is uniformly applied during a period of $T_v = 0.01$ ($t = 46.8$ days) by 10 steps, with the time growth factor (TGF) of 1.1 set afterwards. Note that all the parameters keep the same as in studies[81,84,85] for the convenience of comparison. The results of PFEM with two interpolation schemes (i.e., T3 for pore pressure and T6 for displacement; T3 for both displacement and pore pressure) using the same mesh in Figure 8A are also presented to compare their efficiency and accuracy.

The results of SNS-PFEM in Figures 9 and 11B, D, F are acquired with $\varepsilon_s = 1$ and ε_f in Equation (48). Evolutions of pore pressure and vertical displacement at centre point A, and the distribution of horizontal displacement along section B at the end of consolidation process are presented in Figure 9. All the results of PFEM and SNS-PFEM with regular or distorted mesh agree well with the widely adopted benchmark numerical solutions.[81,84,85] It shows the mesh dependency of SNS-PFEM is not prominent. Figure 10 presents the results of SNS-PFEM with different TGFs in the consolidation stage, which take the total number of time steps as 393, 106, 49 and 36 separately for the same dimensionless time $T_v = 100$. It shows that the accuracy of SNS-PFEM is not influenced by the temporal discretisation. The integration stabilisation coefficient ε_s is then reduced from 1 to 0.0001 corresponding to the NS-PFEM with the regular mesh, leading to the results of Figure 11A, C, E. The contours of total displacement, shear stress and pore pressure in Figure 11 are captured at the end of step 10, when the loading has just finished. These contours are plotted in an extracted window near the footing bottom rather than the whole domain to highlight the comparisons. It can be seen that removing the integration stabilisation technique would produce a sawtooth displacement mode, creating some noise in the distribution of stress and pore pressure. Furthermore, it is discovered that the solution cannot converge if both ε_s and ε_f are set to 0. The stabilisation of pore pressure and NI are necessary in this consolidation problem with material nonlinearity using NS-PFEM.

To further examine the effectiveness of PPP technique when it is approaching the undrained condition, the permeability is reduced to a very low value of $k = 10^{-12}$ m/day, and all the boundaries are set to be impermeable. Since the non-physical

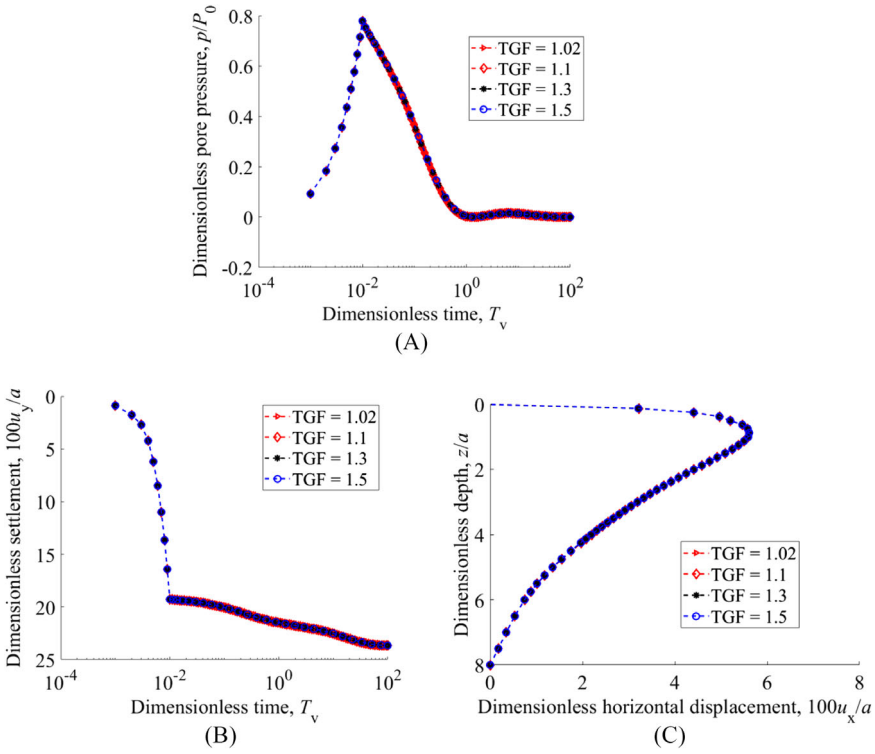

FIGURE 10 (A) Evolution of dimensionless pore pressure at point A; (B) evolution of dimensionless vertical displacement at point A; (C) distribution of dimensionless horizontal displacement with dimensionless depth along the section B of SNS-PFEM with different TGFs. TGF, time growth factor; SNS-PFEM, stabilized node-based smoothed particle finite element method

pressure oscillations is significant under the transient loading (i.e., very short time), only the results of the first time step are plotted to highlight the improved performance of SNS-PFEM with PPP. The contour of pore pressure is recorded in Figure 12A without PPP and in Figure 12B with PPP. As illustrated, the checkboard pattern can be largely alleviated to a reasonable mode when the pressure stabilisation is activated. It visually demonstrates how the PPP can eliminate the spurious oscillation of pore pressure when the undrained incompressible limit is investigated.

To examine the computational efficiency of SNS-PFEM and PFEM, the consumed CPU time and the number of iterations of each step for the simulations in Figure 9 are presented in Figure 13. All simulations are conducted using the same computer with i7-10750H CPU @ 2.60 GHz, 16.0 GB RAM. The number of iterations appears to be a little larger of SNS-PFEM than that of PFEM under the same convergence criterion. This may come from the increased bandwidth of algebraic equation of node-based smoothing construction,[33] and the requirement of numerical stabilisation.[30] Whilst the computational time for SNS-PFEM is less than that of PFEM. In this problem with the same mesh in Figure 8A, the total number of DOF of PFEM (T3p/T6u), PFEM (T3p/T3u) and SNS-PFEM are 11,726, 3990 and 3990 separately. Higher-order interpolation increases the DOFs, and the computational cost rises exponentially as of PFEM (T3p/T6u). The reason why SNS-PFEM is more efficient than PFEM (T3p/T3u) can be summarised as: (1) the NI of SNS-PFEM in this study is organised in an area-weighed approach, avoiding the loop on the quadrature point level; and (2) the cost for variable mapping between nodes and quadrature points for PFEM is not needed. Although all the methods generate accurate results as in Figure 9 and converge in a similar way as in Figure 13B, the computational efficiency of SNS-PFEM seems superior to that of traditional PFEMs.

3.4 | Foundation on a vertical cut

The plane strain problem of foundation on a vertical cut is simulated in this section. The foundation of 5 m width is rigid and pressed vertically into the soil, of which the contact with the soil surface is cohered perfectly. Geometry and boundary conditions are presented in Figure 14A. The movement of the bottom edge of soil in both directions, and the horizontal movement of the right edge are fixed. The top and left boundaries of soil is assumed to be permeable. The soil is simulated using a strain-softening associated MC model,[42,86] with Young's modulus $E = 2000$ kPa and Poisson's ratio $\nu = 0.3$. The friction angle ϕ, dilatancy angle ψ, and cohesion c are reduced with the accumulated equivalent plastic strain (PEEQ) as in the Equations (55)–(57):

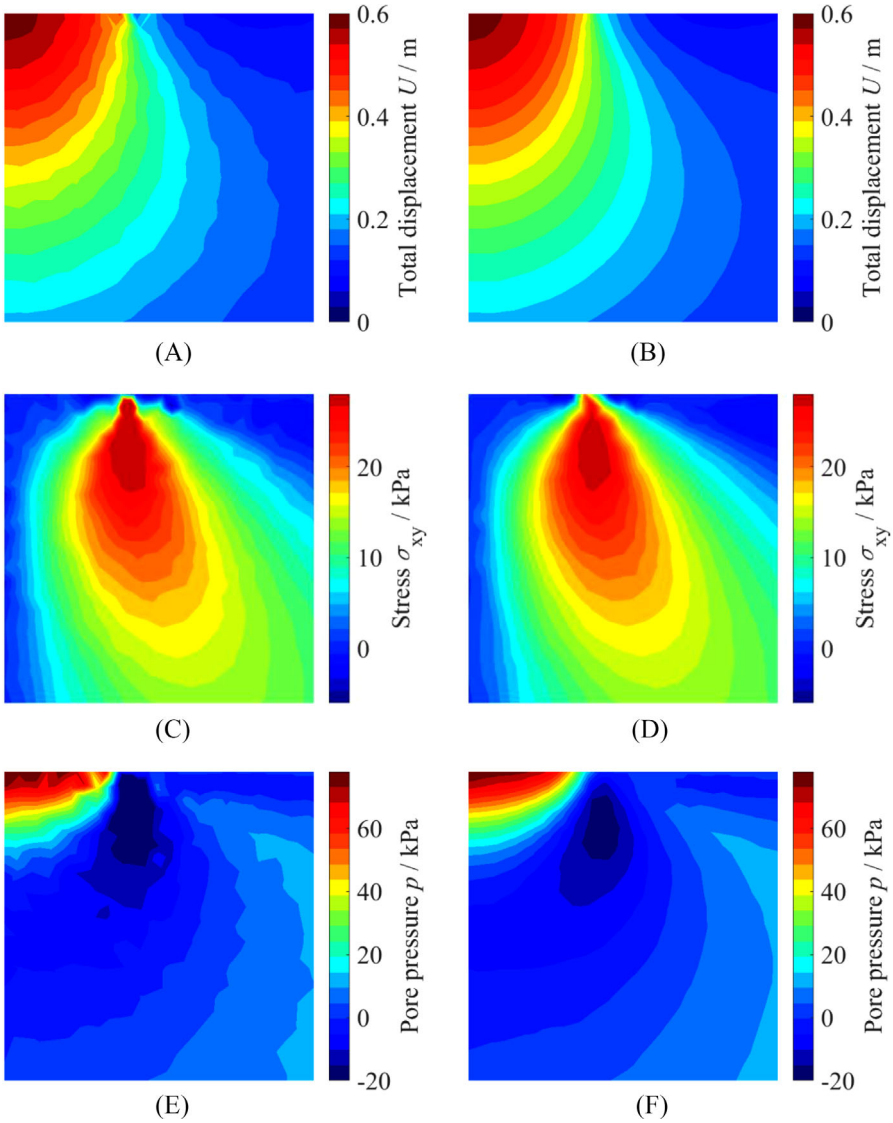

FIGURE 11 Contour of total displacement with (A) NS-PFEM and (B) SNS-PFEM; contour of shear stress with (C) NS-PFEM and (D) SNS-PFEM; contour of pore pressure with (E) NS-PFEM and (F) SNS-PFEM. NS-PFEM, node-based smoothed particle finite element method; SNS-PFEM, stabilized node-based smoothed particle finite element method

$$\phi = \psi = \phi_r + (\phi_p - \phi_r)e^{-\eta\varepsilon_{eq}^p} \tag{55}$$

$$c = c_r + (c_p - c_r)e^{-\eta\varepsilon_{eq}^p} \tag{56}$$

$$\varepsilon_{eq}^p = \sqrt{2(\mathbf{e}^p : \mathbf{e}^p)/3} \tag{57}$$

where $\phi_p = 15°$and $c_p = 25$ kPa are the peak values of friction angle and cohesion; $\phi_r = \phi_p/5$ $c_r = c_p/5$ are the residual values separately. ε_{eq}^p is the equivalent deviatoric plastic strain, with $\mathbf{e}^p$ the plastic deviatoric strain tensor defined in Equation (57). η is the shape factor controlling the strain softening rate. In this study, η takes the value of 3 according to Jin et al.[42] The permeability is set as $k = 10^{-7}$ m/s. The total vertical displacement $U = -0.5$ m is applied within a period of $t = 10^7$ s by 20 steps uniformly. Two types of mesh are generated as in Figure 14B and C to investigate the discretisation dependency of localised strain softening problem. The mesh 1 is generated automatically with a Delaunay triangulation code, and the mesh 2 is constructed based on a 25×25 square lattice. The mesh 2 is biased since the hypotenuse of each element is at an angle of $\pi/4$ with the horizontal axial.

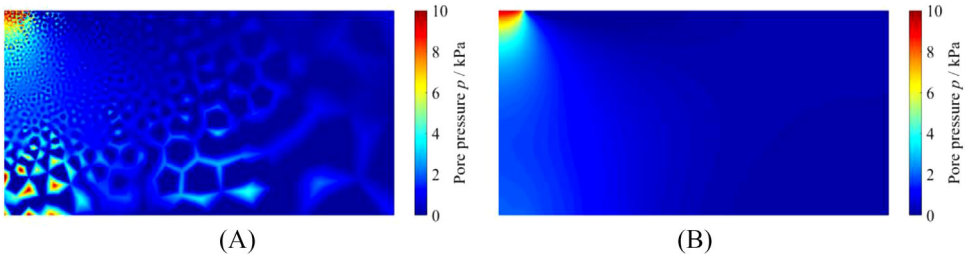

FIGURE 12 Contour of pore pressure in the undrained incompressible limit using (A) SNS-PFEM without PPP; (B) SNS-PFEM with PPP. PPP, polynomial pressure projection; SNS-PFEM, stabilized node-based smoothed particle finite element method

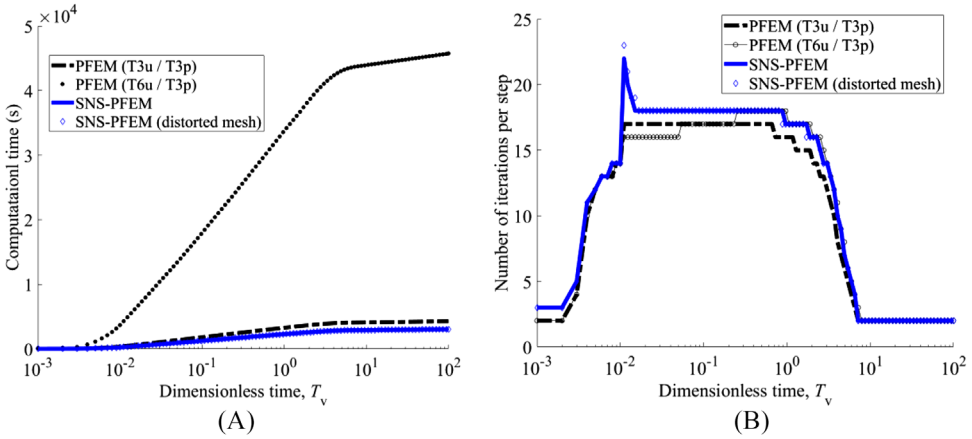

FIGURE 13 Comparison of convergence rate and computational time for PFEM and SNS-PFEM. PFEM, particle finite element method; SNS-PFEM, stabilized node-based smoothed particle finite element method

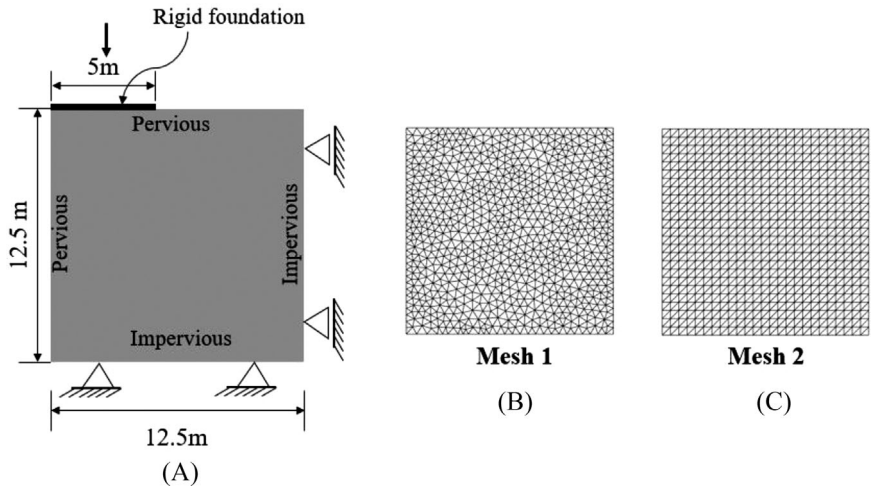

FIGURE 14 Geometry and mesh of foundation on a vertical cut: (A) geometry with boundary conditions; (B) uniform mesh (mesh 1); (C) biased mesh (mesh 2)

Figure 15 exhibits the distribution of equivalent deviatoric plastic strain at the vertical displacement $U = -0.5$ m. A clear shear band is formed in the strain softening soil, indicating the localised failure feature. Figure 16 presents the relationship between vertical displacement and vertical reaction force. Three stages of the curve can be observed as: (1) the reaction force increases linearly with the displacement before yielding; (2) the reaction force decreases with the displacement when the shear band develops, until the localised failure is formed and (3) the reaction force is stable at the level of residual strength, which indicates the movement of a sliding body along the failure plane. Previous study revealed that in a traditional FEM with the biased mesh, the shear band would be influenced by the orientation of element,[87] that is, the shear band will form along the softening direction by the biased mesh, that is, $\pi/4$ in this study as Figure 14C shows. However, with SNS-PFEM the shear bands exhibited in Figure 15 are almost the same from two meshes. Besides, the

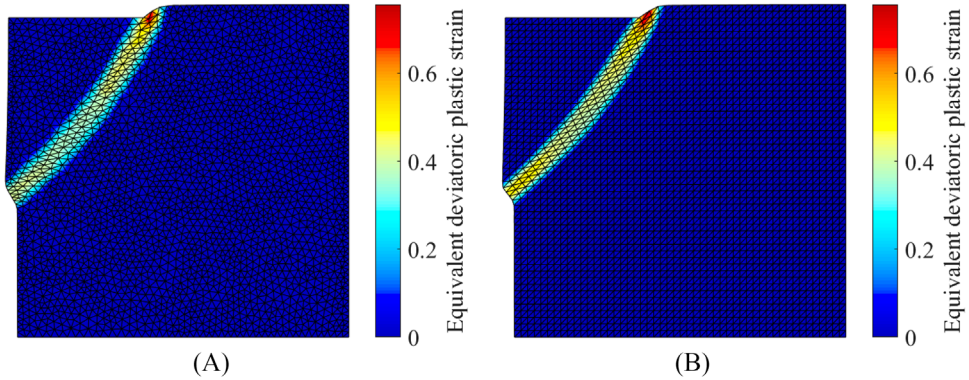

FIGURE 15 Contour of equivalent deviatoric plastic strain with deformed mesh at the end of loading: (A) uniform mesh (mesh 1); (B) biased mesh (mesh 2)

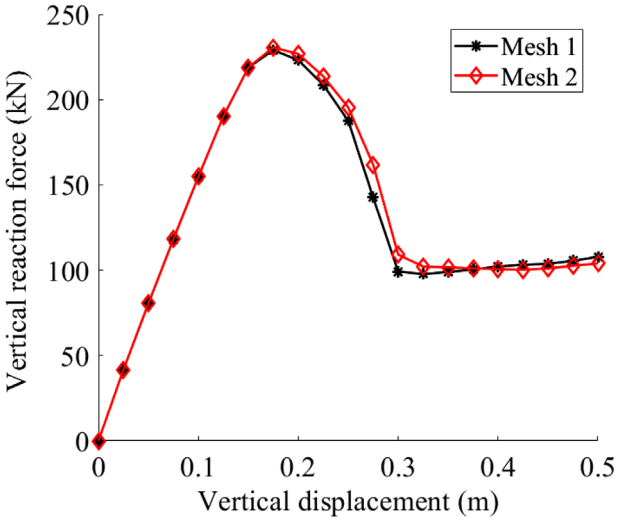

FIGURE 16 Reaction force-vertical displacement curve for the foundation on a vertical cut problem

magnitude of PEEQ and vertical reaction force-displacement curves also agrees well between mesh 1 and mesh 2. All the results demonstrate that the proposed coupled SNS-PFEM is able to simulate the problem of localised failure correctly with low mesh dependency when the strain softening constitutive model is adopted.

4 | LARGE DEFORMATION ANALYSIS OF FOOTING PENETRATION

4.1 | Rigid footing on the Tresca soil

Rigid footing penetration into soft soil is a benchmark test when validating numerical frameworks that involve large deformation, such as FEM-ALE,[14,88,89] MPM,[90] PFEM[91] and SPFEM.[74] When simulating the undrained condition using total stress approach, the Poison's ratio of soil is usually set larger than 0.49.[88–90] However, in the hydromechanical coupled SNS-PFEM, the simulation can be realistically performed with more reasonable Poisson's ratio. In this problem, the huge variation of configuration with mechanical response leads to the coupling of strong geometrical and material nonlinearity.

The discretised half configuration and mesh with load and boundary conditions are presented in Figure 17, with the half-width of strip footing set to $B/2 = 1$ m. A nonuniform mesh of 3729 nodes, 7286 elements is adopted. The weightless soft soil is modelled by Tresca model with Poisson's ratio $\nu = 0.3$ and the cohesion $c_u = 1$ kPa. Different values of Young's modulus E are taken to investigate the influence of the rigidity index I_r on the bearing capacity. The rigidity index I_r is defined as the ratio between the shear modulus G and the cohesion c_u, $I_r = G/c_u = E/(2(1+\upsilon)c_u)$. All the material

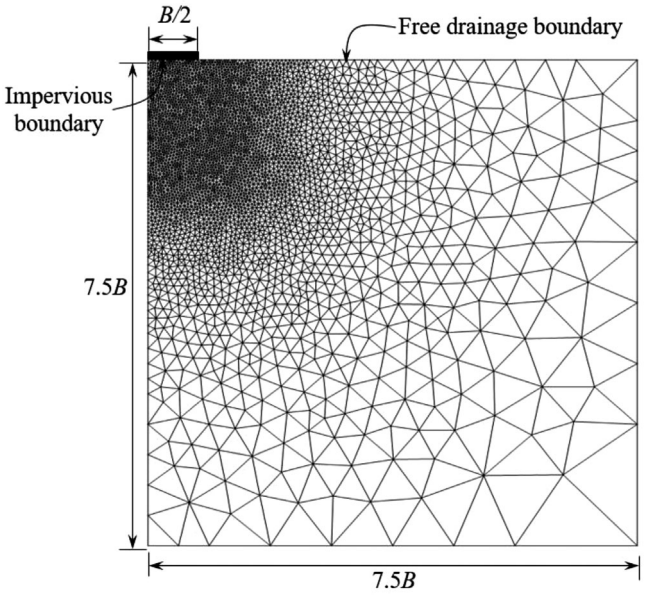

FIGURE 17 Geometry and mesh of strip footing penetration on Tresca soil

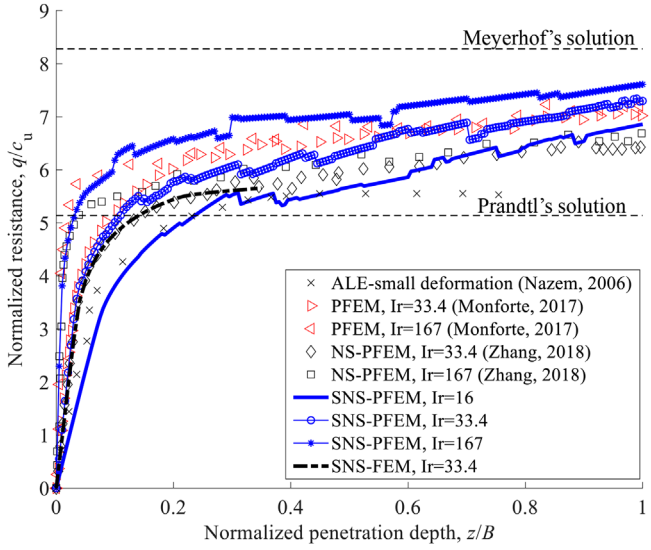

FIGURE 18 Normalised soil resistance-penetration depth curve for strip footing penetration on Tresca soil

properties are set as the normal values for saturated clay. The unit weight of fluid is $\gamma_w = 10$ kN/m^3. The permeability is set as $k = 10^{-9}$ m/day. The dimensionless time is defined as $T_v = \frac{Ekt}{2\gamma_w(1+\nu)(1-2\nu)B^2}$. A uniform vertical displacement of $U = -2$ m is applied to the footing bottom during a short period of $T_v = 1$ by 200 steps. The pore pressure stabilisation is used. All the material properties are set as the common values for saturated clay.

Figure 18 presents the relationship between normalised penetration depth and soil resistance acquired by SNS-PFEM and SNS-FEM, together with several reference solutions of PFEM[91] and NS-PFEM.[44] Prandtl's solution is derived assuming that the footing bottom is placed on the soil surface, with global instability occurring when soil resistance reaches its capacity of $(2 + \pi)\, c_u$.[92] Meyerhof's solution is derived based on a deeply embedded footing model with local failure, leading to the enhanced capacity of $(2 + 2\pi)\, c_u$.[93] When the footing penetrates from the soil surface to a prominent depth, the resistance is believed to transit from the Prandtl's solution to the Meyerhof's solution, even passing through the latter with deep enough penetration.[94] In Figure 18, the result of SNS-FEM based on the initial configuration and fixed mesh is clearly close to the Prandtl's solution at a small penetration, reflecting the small-deformation and un-embedded characteristic of shallow foundation. Whilst as the deformation becomes larger, the result of SNS-FEM is not reliable anymore.

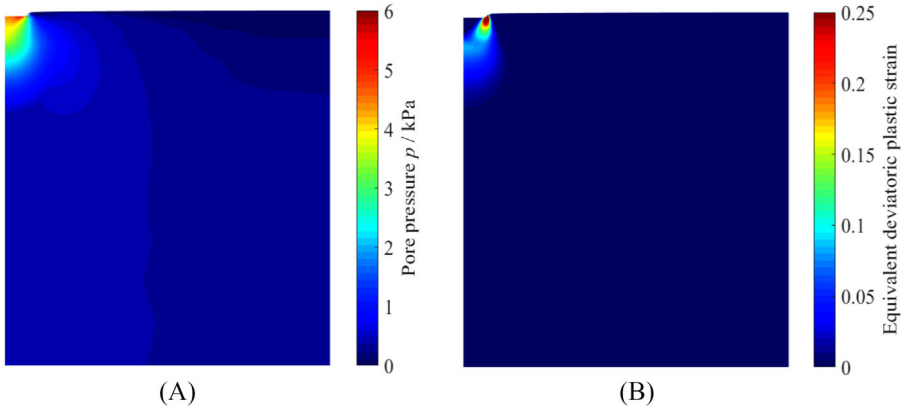

FIGURE 19 Contour of (A) pore pressure; (B) equivalent deviatoric plastic strain at the penetration depth of 0.1 m with stabilized node-based smoothed particle finite element method (SNS-PFEM) (I_r =33.4)

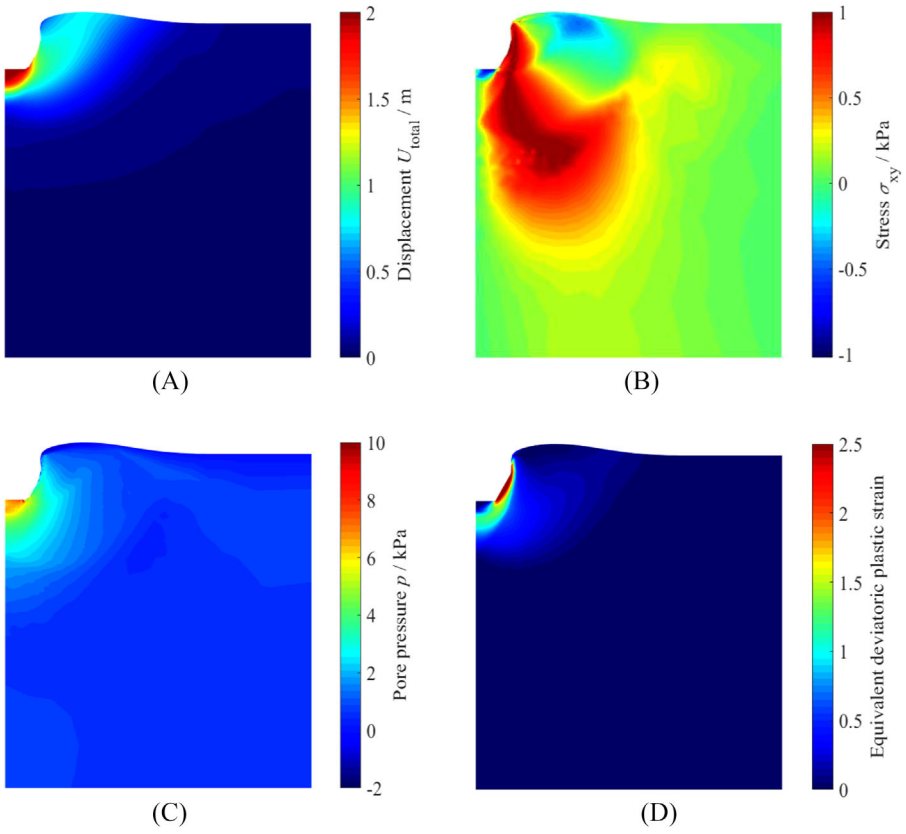

FIGURE 20 Contour of (A) total displacement; (B) shear stress; (C) pore pressure; (D) equivalent deviatoric plastic strain at the penetration depth of 2 m with stabilized node-based smoothed particle finite element method (SNS-PFEM) (I_r =33.4)

The curves of SNS-PFEM, on the other hand, clearly exhibit a transition mode from the lower bound to the upper bound. Results by PFEM, NS-PFEM and SNS-PFEM are very close to each other for the same I_r, especially at the early stage. The SNS-PFEM with a higher rigid index tends to give a stiffer response, whereas the difference becomes smaller as the penetration is deeper. The same trend can also be observed in the results of PFEM[91] and NS-PFEM.[44]

The contours of pore pressure and equivalent deviatoric plastic strain under small deformation are exhibited in Figure 19. As for large deformation, the displacement and pore pressure distribute quite smoothly as in in Figure 20A, C, indicating the correctness of the remeshing scheme. The contour of shear stress in Figure 20B is slightly noising, because rebuilding the node's connectivity changes the stiffness matrix abruptly each time, altering the smoothness of SNS-PFEM

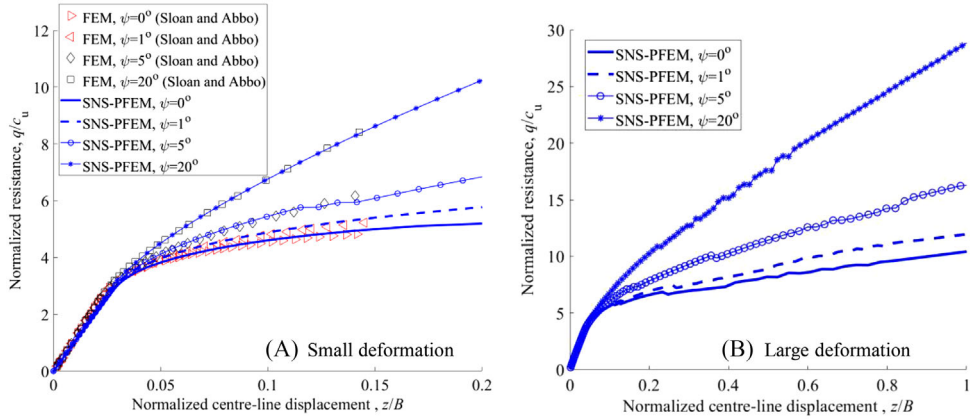

FIGURE 21 Normalised soil resistance – centre line displacement for flexible footing penetration on Mohr–Coulomb soil

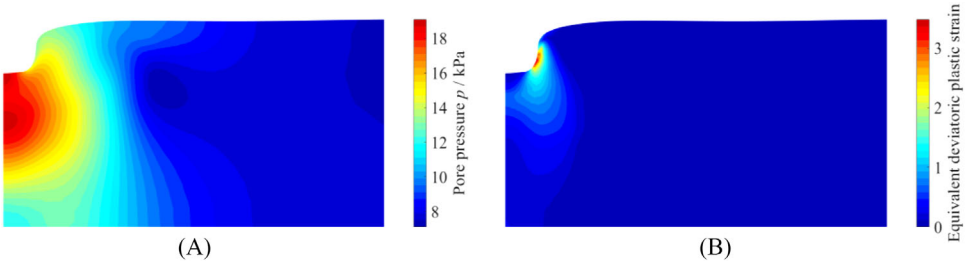

FIGURE 22 Contour of (A) pore pressure; (B) equivalent deviatoric plastic strain with stabilized node-based smoothed particle finite element method (SNS-PFEM) for flexible footing penetration on Mohr–Coulomb soil ($\psi = 1°$)

to a degree. The jump of stiffness in re-meshing is also believed to cause the fluctuation of resistance-displacement curve in Figure 18, which is unavoidable in PFEM-class methods.[74,91] Some rebalancing or smoothing techniques could be considered but lack the physical foundation. The equivalent deviatoric plastic strain is presented in Figure 20D, from which the shear failure band can be clearly captured. The foregoing results prove the correctness and stability of the proposed SNS-PFEM framework in large deformation simulation.

4.2 | Flexible footing on Mohr–Coulomb soil

In this section, a case of undrained strip footing on MC soil presented in Sloan and Abbo[6] is simulated and the large deformation analysis is achieved by increasing the loading. The parameters of MC and the loading settings are the same as those used by Sloan and Abbo.[6] The friction angle is $\phi = 20°$, while the dilatancy angle ψ is set between 0° and 20° to investigate its influence on the mechanical response.[6] The remaining mechanical and hydraulic parameters are listed as follows: Young's modulus $E = 2000$ kPa, Poisson's ratio $\nu = 0.3$, cohesion $c = 10$ kPa, permeability $k = 10^{-5}$ m/s and fluid weight $\gamma_w = 10$ kN/m^3. The same geometry in Figure 8A with a fine mesh of 1947 nodes and 3752 elements is used. All the boundaries are impermeable. The dimensionless loading rate $\omega = \Delta P/c\Delta T_v$ is set to 150, based on which the total time of penetration is 28.08 days. As Figure 21A shows, the curves of soil resistance-displacement of SNS-PFEM agree well with the FEM solutions at the small deformation stage. When the penetration goes deeper, the SNS-PFEM can also predict a reasonable result as shown in Figure 21B, which is similar to the results in Figure 18. As Sloan and Abbo[6] reported, for the Biot's formulation with MC soil used in this study, the non-zero dilation angle can cause a drop in the excess pore water pressure and thus increase the shear strength, leading to a hardening effect. This phenomenon is well reflected by the proposed coupled SNS-PFEM when the deformation becomes large. Figure 22 exhibits the distributions of pore pressure and equivalent deviatoric plastic strain the large deformation condition (at $z/B = 1$). The contour of excess pore water pressure is still smooth, indicating the effectiveness of PPP stabilisation technique. Therefore, all the comparisons demonstrate the proposed coupled SNS-PFEM also performs well in simulating the large deformation on MC soil.

5 | CONCLUSIONS

A stabilised node-based particle finite element method (SNS-PFEM), together with the PPP technique, has been proposed and implemented for hydromechanical coupled problems. Closed formulations for PPP and stable NI were derived in the node-based smoothed T3 interpolation scheme to boost the computational stability and efficiency.

Four benchmark tests were conducted: 1D Terzaghi's consolidation, Mandel's problem, strip footing consolidation in MC soil and foundation on a vertical cut. The results of the SNS-PFEM agreed well with all previous reference solutions. The ability of PPP to cure spurious pressure oscillation under nearly undrained conditions was validated in two cases. The advantages of stabilised NI were demonstrated by comparison with simulations using NS-PFEM. The computational efficiency of SNS-PFEM was also demonstrated by solving the same problems using other coupled PFEMs and comparing the CPU time consumed. Finally, the large deformation analysis of strip footing penetration into saturated soft soil was simulated. Reasonable results for resistance–displacement curve and failure mode of soil could be observed, showing the strength of a remeshing strategy under conditions of strong geometrical nonlinearity. The proposed SNS-PFEM is thus believed to deal with conditions of low to high permeability, short and long period and small and large deformation uniformly and efficiently.

Future works will focus on the improvement of SNS-PFEM in two aspects: (1) extending the current SNS-PFEM to 3D version. The 4-node linear tetrahedron element (T4) will be adopted, which shares many essential mathematical features with T3 element, thus most advantages of 2D SNS-PFEM can be preserved in the 3D conditions; (2) applying the proposed SNS-PFEM to more complex geotechnical practices, relating to the contact modelling of soil–structure interactions and advanced soil constitutive models.

ACKNOWLEDGEMENTS

This research was financially supported by the Research Grants Council (RGC) of Hong Kong Special Administrative Region Government (HKSARG) of China (Grant No.: 15209119, R5037-18F), The Hong Kong Polytechnic University Strategic Importance Fund (ZE2T) and Project of Research Institute of Land and Space (CD78).

DATA AVAILABILITY STATEMENT

The data that support the findings of this study are available from the corresponding author through Email upon reasonable request.

REFERENCES

1. Karstunen M, Yin ZY. Modelling time-dependent behaviour of Murro test embankment. *Géotechnique*. 2010;60(10):735-749.
2. Leshchinsky B, Vahedifard F, Koo HB, Kim SH. Yumokjeong Landslide: an investigation of progressive failure of a hillslope using the finite element method. *Landslides*. 2015;12(5):997-1005.
3. Yang J, Yin ZY, Laouafa F, Hicher PY. Internal erosion in dike-on-foundation modeled by a coupled hydromechanical approach. *Int J Numer Anal Methods Geomech*. 2019;43(3):663-683.
4. Yang J, Yin ZY, Laouafa F, Hicher PY. Three-dimensional hydromechanical modeling of internal erosion in dike-on-foundation. *Int J Numer Anal Methods Geomech*. 2020;44(8):1200-1218.
5. Zhang X, Sheng DC, Sloan SW, Krabbenhoft K. Second-order cone programming formulation for consolidation analysis of saturated porous media. *Comput Mech*. 2016;58(1):29-43.
6. Sloan SW, Abbo AJ. Biot consolidation analysis with automatic time stepping and error control Part 2: applications. *Int J Numer Anal Methods Geomech*. 1999;23(6):493-529.
7. Sloan SW, Abbo AJ. Biot consolidation analysis with automatic time stepping and error control Part 1: theory and implementation. *Int J Numer Anal Methods Geomech*. 1999;23(6):467-492.
8. Manoharan N, Dasgupta SP. Consolidation analysis of elastoplastic soil. *Comput Struct*. 1995;54(6):1005-1021.
9. Zhang Q, Yan X, Shao JL. Fluid flow through anisotropic and deformable double porosity media with ultra-low matrix permeability: a continuum framework. *J Pet Sci Eng*. May 2021;200(11):108349.
10. Zhang Q, Yan X, Li ZH. A mathematical framework for multiphase poromechanics in multiple porosity media. *Comput Geotech*. 2022;146:104728.
11. Liu G-R, Quek SS. *The Finite Element Method: A Practical Course*. Butterworth-Heinemann; 2013.
12. Belytschko T, Liu WK, Moran B, Elkhodary K. *Nonlinear Finite Elements for Continua and Structures*. John Wiley & Sons; 2013.
13. Hughes TJ. *The Finite Element Method: Linear Static and Dynamic Finite Element Analysis*. Courier Corporation; 2012.
14. Bathe K-J. *Finite Element Procedures*. Prentice-Hall; 1996.
15. Hua LN. Stable element-free Galerkin solution procedures for the coupled soil-pore fluid problem. *Int J Numer Methods Eng*. 2011;86(8):1000-1026.

16. Khoshghalb A, Khalili N. A stable meshfree method for fully coupled flow-deformation analysis of saturated porous media. *Comput Geotech*. 2010;37(6):789-795.
17. Samimi S, Pak A. Three-dimensional simulation of fully coupled hydro-mechanical behavior of saturated porous media using Element Free Galerkin (EFG) method. *Comput Geotech*. 2012;46:75-83.
18. Wei HY, Chen JS, Beckwith F, Baek J. A naturally stabilized semi-Lagrangian meshfree formulation for multiphase porous media with application to landslide modeling. *J Eng Mech*. 2020;146(4):04020012.
19. Wei HY, Chen JS, Hillman M. A stabilized nodally integrated meshfree formulation for fully coupled hydro-mechanical analysis of fluid-saturated porous media. *Comput Fluids*. 2016;141:105-115.
20. Zeng W, Liu GR. smoothed finite element methods (S-FEM): an overview and recent developments. *Arch Comput Methods Eng*. 2018;25(2):397-435.
21. Chen J-S, Hillman M, Chi S-W. Meshfree methods: progress made after 20 years. *J Eng Mech*. 2017;143(4):04017001.
22. Liu GR. On G space theory. *Int J Comput Methods*. 2009;6(2):257-289.
23. Liu GR. A G space theory and a weakened weak (W-2) form for a unified formulation of compatible and incompatible methods: part II applications to solid mechanics problems. *Int J Numer Methods Eng*. 2010;81(9):1127-1156.
24. Liu GR. A G space theory and a weakened weak (W2) form for a unified formulation of compatible and incompatible methods. *Part I theory*. 2010;81(9):1093-1126. https://doi.org/10.1002/nme.2719
25. Mabssout M, Pastor M. A two-step Taylor-Galerkin algorithm applied to shock wave propagation in soils. *Int J Numer Anal Methods Geomech*. 2003;27(8):685-704.
26. Zienkiewicz OC, Taylor RL. *The Finite Element Method*. vol. 2. McGraw-Hill; 1991.
27. Zienkiewicz OC, Taylor RL. *The Finite Element Method*. vol. 1. McGraw-Hill; 1989.
28. Cervera M, Chiumenti M, Codina R. Mixed stabilized finite element methods in nonlinear solid mechanics part II: strain localization. *Comput Method Appl Mech Eng*. 2010;199(37-40):2571-2589.
29. Cervera M, Chiumenti M, Codina R. Mixed stabilized finite element methods in nonlinear solid mechanics part I: formulation. *Comput Method Appl Mech Eng*. 2010;199(37-40):2559-2570.
30. Puso MA, Chen JS, Zywicz E, Elmer W. Meshfree and finite element nodal integration methods. *Int J Numer Meth Eng*. 2008;74(3):416-446.
31. Puso MA, Solberg J. A stabilized nodally integrated tetrahedral. *Int J Numer Meth Eng*. 2006;67(6):841-867.
32. Chen JS, Wu CT, Yoon S, You Y. A stabilized conforming nodal integration for Galerkin mesh-free methods. *Int J Numer Methods Eng*. 2001;50(2):435-466.
33. Liu G-R, Trung NT. *Smoothed Finite Element Methods*. CRC Press; 2016.
34. Nguyen-Xuan H, Liu GR. An edge-based smoothed finite element method softened with a bubble function (bES-FEM) for solid mechanics problems. *Comput Struct*. 2013; 128:14-30.
35. Jiang C, Han X, Liu GR, Zhang ZQ, Yang G, Gao GJ. Smoothed finite element methods (S-FEMs) with polynomial pressure projection (P3) for incompressible solids. *Eng Anal Bound Elem*. 2017;84:253-269.
36. Ghaffaripour O, Esgandani GA, Khoshghalb A, Shahbodaghkhan B. Fully coupled elastoplastic hydro-mechanical analysis of unsaturated porous media using a meshfree method. *Int J Numer Anal Methods Geomech*. 2019;43(11):1919-1955.
37. Ghaffaripour O, Khoshghalb A, Khalili N. An edge-based smoothed point interpolation method for elasto-plastic coupled hydro-mechanical analysis of saturated porous media. *Comput Geotech*. 2017;82:99-109.
38. Khoshghalb A, Shafee A. Does the upper bound solution property of the Node-based Smoothed Point Interpolation Methods (NSPIMs) hold true in coupled flow-deformation problems of porous media? *Comput Geotech*. 2021;133:104016.
39. Shafee A, Khoshghalb A. An improved node-based smoothed point interpolation method for coupled hydro-mechanical problems in geomechanics. *Comput Geotech*. 2021;139:104415.
40. Zhang W, Zhong ZH, Peng C, Yuan WH, Wu W. GPU-accelerated smoothed particle finite element method for large deformation analysis in geomechanics. *Comput Geotech*. 2021;129:13.
41. Jin YF, Yin ZY, Zhou XW, Liu FT. A stable node-based smoothed PFEM for solving geotechnical large deformation 2D problems. *Comput Method Appl Mech Eng*. 2021;387:114179.
42. Jin YF, Yin ZY, Yuan WH. Simulating retrogressive slope failure using two different smoothed particle finite element methods: a comparative study. *Eng Geol*. 2020;279:105870.
43. Yuan WH, Wang B, Zhang W, Jiang Q, Feng XT. Development of an explicit smoothed particle finite element method for geotechnical applications. *Comput Geotech*. 2019;106:42-51.
44. Zhang W, Yuan WH, Dai BB. Smoothed particle finite-element method for large-deformation problems in geomechanics. *Int J Geomech*. 2018;18(4):04018010.
45. Chen JS, Wu CT, Yoon S, YJIjfnmie You. A stabilized conforming nodal integration for Galerkin mesh-free methods. *Int J Numer Methods Eng*. 2001;50(2):435-466.
46. Feng H, Cui XY, Li GY. A stable nodal integration method with strain gradient for static and dynamic analysis of solid mechanics. *Eng Anal Bound Elem*. 2016;62:78-92.
47. Li Y, Liu GR. A novel node-based smoothed finite element method with linear strain fields for static, free and forced vibration analyses of solids. *Appl Math Comput*. 2019;352:30-58.
48. Vo-Minh T, Nguyen-Son L. A stable node-based smoothed finite element method for stability analysis of two circular tunnels at different depths in cohesive-frictional soils. *Comput Geotech*. 2021;129:103865.

49. Yang H, Cui XY, Li S, Bie YH. A stable node-based smoothed finite element method for metal forming analysis. *Comput Mech*. 2019;63(6):1147-1164.
50. Wu CT, Wu Y, Liu Z, Wang D. A stable and convergent Lagrangian particle method with multiple nodal stress points for large strain and material failure analyses in manufacturing processes. *Finite Elem Anal Des*. 2018;146:96-106.
51. Haga JB, Osnes H, Langtangen HP. On the causes of pressure oscillations in low-permeable and low-compressible porous media. *Int J Numer Anal Methods Geomech*. 2012;36(12):1507-1522.
52. Zhao YD, Choo J. Stabilized material point methods for coupled large deformation and fluid flow in porous materials. *Comput Method Appl Mech Eng*. 2020;362:112742.
53. Brezzi F, Bathe KJ. A discourse on the stability conditions for mixed finite-element formulations. *Comput Method Appl Mech Eng*. 1990;82(1-3):27-57.
54. White JA, Borja RI. Stabilized low-order finite elements for coupled solid-deformation/fluid-diffusion and their application to fault zone transient. *Comput Method Appl Mech Eng*. 2008;197(49-50):4353-4366.
55. Hafez M, Soliman M. IN: AIAA Computational Fluid Dynamics Conference, 10th, Honolulu, HI, June 24–27, 1991, Technical Papers (A91–40701 17–34). Washington, DC, American Institute of Aeronautics and Astronautics, 1991, p. 368–379.
56. Onate E. A stabilized finite element method for incompressible viscous flows using a finite increment calculus formulation. *Comput Method Appl Mech Eng*. 2000;182(3-4):355-370.
57. Preisig M, Prevost JH. Stabilization procedures in coupled poromechanics problems: a critical assessment. *Int J Numer Anal Methods Geomech*. 2011;35(11):1207-1225.
58. Wan J. *Stabilized Finite Element Methods for Coupled Geomechanics and Multiphase Flow*. Stanford University; 2003.
59. Pastor H, Li T, Liu X, Zienkiewicz OC, Quecedo M. A fractional step algorithm allowing equal order of interpolation for coupled analysis of saturated soil problems. *Mech Cohes-Frict Mater*. 2000;5(7):511-534.
60. Mira P, Pastor M, Li T, Liu X. A new stabilized enhanced strain element with equal order of interpolation for soil consolidation problems. *Comput Method Appl Mech Eng*. 2003;192(37-38):4257-4277.
61. Bochev PB, Dohrmann CR, Gunzburger MD. Stabilization of low-order mixed finite elements for the Stokes equations. *SIAM J Numer Anal*. 2006;44(1):82-101.
62. Smith IM, Griffiths DV, Margetts L. *Programming the Finite Element Method*. John Wiley & Sons; 2013.
63. Wu CT, Hu W. A two-level mesh repartitioning scheme for the displacement-based lower-order finite element methods in volumetric locking-free analyses. *Comput Mech*. 2012;50(1):1-18.
64. Liu GR, Nguyen-Thoi T, Lam KY. An edge-based smoothed finite element method (ES-FEM) for static, free and forced vibration analyses of solids. *J Sound Vib*. 2009;320(4):1100-1130.
65. Beissel S, Belytschko T. Nodal integration of the element-free Galerkin method. *Comput Methods Appl Mech Eng*. 1996;139:49-74.
66. Randles P, Libersky L, Petschek A. *On Neighbors, Derivatives, and Viscosity in Particle Codes*. Los Alamos National Lab.; 1999.
67. Choo J, Borja RI. Stabilized mixed finite elements for deformable porous media with double porosity. *Comput Method Appl Mech Eng*. 2015;293:131-154.
68. Jin YF, Yin ZY, Li J, Dai JG. A novel implicit coupled hydro-mechanical SPFEM approach for modelling of delayed failure of cut slope in soft sensitive clay. *Comput Geotech*. 2021;140:104474.
69. Sun WC, Ostien JT, Salinger AG. A stabilized assumed deformation gradient finite element formulation for strongly coupled poromechanical simulations at finite strain. *Int J Numer Anal Methods Geomech*. 2013;37(16):2755-2788.
70. Zhang Q, Borja RI. Poroelastic coefficients for anisotropic single and double porosity media. *Acta Geotech*. 2021;16(10):3013-3025.
71. Monforte L, Navas P, Carbonell JM, Arroyo M, Gens A. Low-order stabilized finite element for the full Biot formulation in soil mechanics at finite strain. *Int J Numer Anal Methods Geomech*. 2019;43(7):1488-1515.
72. Zhao Y, Borja RI. Anisotropic elastoplastic response of double-porosity media. *Comput Method Appl Mech Eng*. 2021;380:32.
73. Carbonell JM, Onate E, Suarez B. Modeling of ground excavation with the particle finite-element method. *J Eng Mech*. 2010;136(4):455-463.
74. Jin YF, Yuan WH, Yin ZY, Cheng YM. An edge-based strain smoothing particle finite element method for large deformation problems in geotechnical engineering. *Int J Numer Anal Methods Geomech*. 2020;44(7):923-941.
75. Zhang X, Krabbenhoft K, Sheng DC, Li WC. Numerical simulation of a flow-like landslide using the particle finite element method. *Comput Mech*. 2015;55(1):167-177.
76. Zhang X, Onate E, Torres SAG, Bleyer J, Krabbenhoft K. A unified Lagrangian formulation for solid and fluid dynamics and its possibility for modelling submarine landslides and their consequences. *Comput Methods Appl Mech Eng*. 2019;343:314-338.
77. Zhang X, Ding YT, Sheng DC, Sloan SW, Huang WX. Quasi-static collapse of two-dimensional granular columns: insight from continuum modelling. *Granul Matter*. 2016;18:41. https://doi.org/10.1007/s10035-016-0643-z
78. Zhang X, Wang L, Krabbenhoft K, Tinti S. A case study and implication: particle finite element modelling of the 2010 Saint-Jude sensitive clay landslide. *Landslides*. 2020;17(5):1117-1127.
79. Mandel J. Consolidation des sols (étude mathématique). *Géotechnique*. 1953;73:287-299.
80. Terzaghi K, Peck RB, Mesri G. *Soil Mechanics*. John Wiley and Sons; 1996.
81. Sabetamal H, Nazem M, Sloan SW, Carter JP. Frictionless contact formulation for dynamic analysis of nonlinear saturated porous media based on the mortar method. *Int J Numer Anal Methods Geomech*. 2016;40(1):25-61.
82. Verruijt AJ. *Theory and Problems of Poroelasticity*. Delft University of Technology; 2016.

83. Cheng AHD, Detournay E. A direct boundary element method for plane-strain poroelasticity. *Int J Numer Anal Methods Geomech*. 1988;12(5):551-572.
84. Manoharan N, Dasgupta SP. Consolidation analysis of elasto-plastic soil. *Comput Struct*. 1995;54(6):1005-1021.
85. Ghaffaripour O, Khoshghalb A, Khalili N. An edge-based smoothed point interpolation method for elasto-plastic coupled hydro-mechanical analysis of saturated porous media. *Comput Geotech*. 2017;82(1):99-109.
86. Soga K, Alonso E, Yerro A, Kumar K, Bandara S. Trends in large-deformation analysis of landslide mass movements with particular emphasis on the material point method. *Geotechnique*. 2016;66(3):248-273.
87. Callari C, Armero F. Finite element methods for the analysis of strong discontinuities in coupled poro-plastic media. *Comput Method Appl Mech Eng*. 2002;191(39-40):4371-4400.
88. Kardani M, Nazem M, Carter JP, Abbo AJ. Efficiency of High-order elements in large-deformation problems of geomechanics. *Int J Geomech*. 2015;15(6):04014101. https://doi.org/10.1061/(ASCE)GM.1943-5622.0000457
89. Nazem M, Sheng DC, Carter JP. Stress integration and mesh refinement for large deformation in geomechanics. *Int J Numer Meth Eng*. 2006;65(7):1002-1027.
90. Solowski WT, Sloan SW. Evaluation of material point method for use in geotechnics. *Int J Numer Anal Methods Geomech*. 2015;39(7):685-701.
91. Monforte L, Arroyo M, Carbonell JM, Gens A. Numerical simulation of undrained insertion problems in geotechnical engineering with the Particle Finite Element Method (PFEM). *Comput Geotech*. 2017;82:144-156.
92. Prandtl L. Hauptaufsätze: Über die Eindringungsfestigkeit (Härte) plastischer Baustoffe und die Festigkeit von Schneiden. *Z Angew Math Mech*. 1921;1(1):15-20.
93. Meyerhof GJG. The ultimate bearing capacity of foudations. *Géotechnique*. 1951;2(4):301-332.
94. Da Silva MV, Krabbenhoft K, Lyamin AV, Sloan SW. *Rigid-Plastic Large-Deformation Analysis of Geotechnical Penetration Problems*. University of New South Wales (UNSW), Centre for Infrastructure Engineering and Safety (CIES); 2011.

How to cite this article: Wang Z-Y, Jin Y-F, Yin Z-Y, Wang Y-Z. A novel coupled NS-PFEM with stable nodal integration and polynomial pressure projection for geotechnical problems. *Int J Numer Anal Methods Geomech*. 2022;46:2535–2560. https://doi.org/10.1002/nag.3417